Physics impacts of DAQ and trigger systems on large-scale hadron collider experiments and a control and monitoring scheme to achieve the impact

Kosei Yamakawa

3rd March, 2022

Abstract

Particle physics has advanced along with the technological improvements of experimental equipment, especially the increase of center-of-mass energy provided by accelerators, since the early 20th century. The large hadron collider (LHC), the world's largest accelerator ever, has started in 2009. The center-of-mass energy, the proton beam bunch crossing rate, and the Pb-Pb collision rate are 14 TeV, 40 MHz, and 50 kHz, respectively, in the LHC Run 3 starting from 2022. For the next decade, it is not easy to increase the center-of-mass energy with a larger circular collider than the LHC mainly due to a financial reason. Luminosity upgrade is only realistic as improvements of accelerators. The LHC will be upgraded to the high-luminosity LHC (HL-LHC) providing a factor of ten larger luminosity than the current value, in 2028.

The following physics missions are addressed with the LHC and the HL-LHC. First, tests of the standard model should be performed by the measurements of Higgs couplings with quarks and leptons as usual as self-coupling of Higgs. The *CP* violation measurements via rare heavy flavor hadron decays can also contribute to the standard model tests. In addition, new physics searches such as supersymmetry (SUSY) particle search are conducted. The heavy-ion program is another major task with the LHC to explore the QGP properties. A new trigger and data acquisition is crucial to accomplish the above physics missions with the benefit of high luminosity.

All collision event collection is ideal in hadron collider experiments. However, computing power and a storage cost prevented the implementation of all collision event collection until now. Thus, trigger-based readout systems have been commonly used to maximize the experimental performance with reasonable data size. Recent technical innovations, such as high-performance CPUs and a large amount of storage with low costs, allow us to introduce a continuous readout system. Nonetheless, a recording of all collision events is not realistic even in the current situation. An effective online data reduction must be implemented to realize a continuous readout.

The four LHC experiments, ALICE, LHCb, ATLAS, and CMS upgrade their trigger and data acquisition systems to achieve their physics goals with the LHC and the HL-LHC. ALICE and LHCb employ continuous readout systems. ALICE makes a lot of efforts to have data reduction by online data reconstruction and calibration with detector conditions to record Pb-Pb collision events as much as possible. Similarly, LHCb selects their interested event candidates with a temporary recording of whole *pp* collision events by utilizing a characteristic decay topology of heavy flavor hadron decays more efficiently compared to selections of its high-level hardware trigger which have the trigger rate limitation of 1 MHz technically. On the other hand, it is more challenging to have continuous readout systems for ATLAS and CMS, which aim to take data with the higher luminosity of the HL-LHC. Hardware trigger systems are still employed because their trigger systems have room for improvements, then faster high-level hardware triggers can meet their requirements with reasonable efforts to pick up the energetic events in which their target particles such as Higgs bosons and SUSY particles are generated. However, their trigger rates are close to the limitation and continuous readout systems can be the best choice for any experiments. Further technology innovations will allow to record all collision data with continuous readout systems even with much higher luminosity.

As discussed above, we should aim to realize continuous readout systems in any hadron collider experiments. ALICE is one of the frontiers in this field. Data reduction must be done for a continuous readout. Online calibration and reconstruction with considering detector conditions are crucial in the new ALICE readout system. The control and monitoring system for sub-detectors was separated from the physics data processing system in the previous readout system. However, the detector condition data such as temperature, pressure, inactive regions, and so on are important inputs for calibration and reconstruction. In the new system, they come along with raw data of sub-detectors in the same data stream so that the online calibration and reconstruction is done more efficiently. As a result, the processing data size can be significantly reduced by a factor of seven at the calibration stage and an additional factor of five at the reconstruction stage. Finally, the reduced data can be stored in a data storage for offline data processing. The continuous readout system increases the physics performance of ALICE by a significant improvement of the data collection capability.

The new system has been demonstrated with the Muon Forward Tracker (MFT), newly installed in the ALICE detector from the coming runs. The MFT detector control system is designed and developed from scratch based on the new control and monitoring scheme. The new control scheme is a model case for a continuous readout system and online data reductions.

Contents

List of Figures

List of Tables

Preface

This thesis is composed of two halves. In Part I, the upgrade strategies of trigger and data acquisition systems at the large-scale hadron collider experiments and their physics impacts are described. First chapter explains that the progress of the modern particle physics with the technical innovations. The physics tasks to be addressed with a hadron collider are described in Chap. 2. Next, it is expressed that the strategies of the large hadron collider experiments. Chapter 4 summarize the strategies and discuss a trend of trigger and data acquisition systems.

In Part II, the detector control system for the new detector, following the strategy at ALICE is described. Chapter 1 is the introduction of the new control scheme to achieve the physics goals described in Part I. The second chapter explains the concept and setup of new detector. The design of the control system for the MFT is described in Chap. 3. Finally, the conclusion of the thesis including the contents of Part I is described in Chap. 4.

Part I

Data Acquisition and Physics Impact in the Large-Scale Hadron Collider Experiments

Chapter 1

Introduction

In this chapter, how modern particle physics has been established with the technical improvements of accelerators and detectors are described firstly.

1.1 Modern particle physics with the evolution of experimental technologies

Particle physics has progressed with the improvements of experimental technologies, particularly accelerators from the early 20th century. Figure 1.1 shows the growth of the center-of-mass collision energy. Filled markers are fixed-target experiments and round markers are collider experiments. The standard model, which describes strong, weak, and electromagnetic interactions and includes the quark model, has been established with the experiments using the accelerators. Here, the center-of-mass collision energy, $\sqrt{s}$, is defined

$$\sqrt{s} = \sqrt{(E_1 + E_2)^2 - (\boldsymbol{p}_1 c + \boldsymbol{p}_2 c)^2} \tag{1.1}$$

where four-momenta of the colliding particle 1 and the colliding particle 2 are $p_1 = (E_1; \boldsymbol{p}_1)$ and $p_2 = (E_2; \boldsymbol{p}_2)$, respectively.
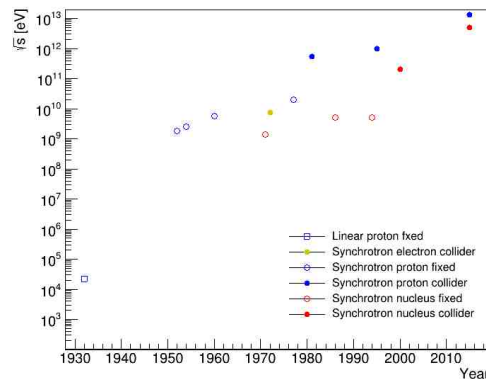
Figure 1.1: The evolution of the center-of-mass energy of the accelerators.

1.1.1 Particle physics and experimental technologies in the early days

In the history of detectors, the first impact was made by the invention of a cloud chamber by Charles Thomson Rees Wilson. It enabled us to see radiation rays for the first time. When a charged particle passes inside supersaturation state gas in a chamber, fog drips are produced along the particle path. Anderson discovered a theoretically predicted positron, which is an antiparticle of the electron, using a cloud chamber in 1932. He also discovered a muon in 1935. This is an example that a new technology progresses particle physics.

The accelerator developed by Cockcroft and Walton was the electrostatic system and accelerated protons to an energy of 700 keV ($\sqrt{s} \sim$ 22 keV) in 1932. They made the first nuclear reaction p + ^{7}Li $\rightarrow$ ^{4}He + ^{4}He with the accelerating protons. Van de Graaff also developed the accelerator, which was an electrostatic system in the 1930s. The electrostatic accelerators have a limit of accelerating energy at around $O(10)$ MeV.

The second revolution was the invention of a cyclotron. Figure 1.2 shows the general view of classical cyclotrons. A cyclotron is composed of an electric magnet and two accelerating electrodes, called *Dees*, in a vacuum chamber. The magnet generates a uniform magnetic field, B in units of T, which is perpendicular to the accelerating electrode. A radio frequency power (RF) is supplied to the Dees. An ion source is located at the center of the chamber and charged particles are accelerated whenever the particle passes the gap. The particles exit the chamber when a rotation radius, R in units of m, is equal to a radius of the chamber. The radius R in the uniform field, B, is written as

$$\frac{mv^2}{R} = evB \tag{1.2}$$

$$R = \frac{\gamma mv}{eB} = \frac{mv}{eB\sqrt{1 - (v^2/c^2)}}. \tag{1.3}$$

Here, m, e, and v mean rest mass (in GeV/c^2), charge, and velocity of the particle. The radius R is proportional to the momentum of the particle, therefore, a large magnet is needed to achieve higher energies. Rotation frequency, ω, is

$$\omega = 2\pi \frac{v}{2\pi R} = \frac{eB}{\gamma m}. \tag{1.4}$$

In the non-relativistic case ($v << c$), ω is fixed because a particle mass is constant. However, a particle's mass depends on the velocity in the relativistic energy. Hence, ω is not constant and it is difficult to synchronize the radio frequency with the rotation frequency to accelerate charged particles. The maximum energy of accelerated protons is around 20 MeV in the case of classical cyclotrons. Transuranium elements including neptunium were synthesized using the classical cyclotrons in the 1940s.

The synchrotron principle was invented by Veksler and McMillan independently in 1945. They solved the synchronization of a rotation period and a radio frequency. An accelerated beam trajectory is fixed and a magnetic field is changed stronger according to the accelerated energies. Electromagnets are small because they are located around the trajectory. Longitudinal oscillations of accelerated particles occur. The phase stability was considered to solve longitudinal oscillations. Figure 1.3 shows a general view of the phase stability. Here, O and O' are synchronous particles with a radio frequency and run in a rotation period of T_{rf}. The particle A coming from behind the particle O is accelerated with a lower accelerating electric field than the particle O. The particle A places a point A' closer to the synchronous point O'
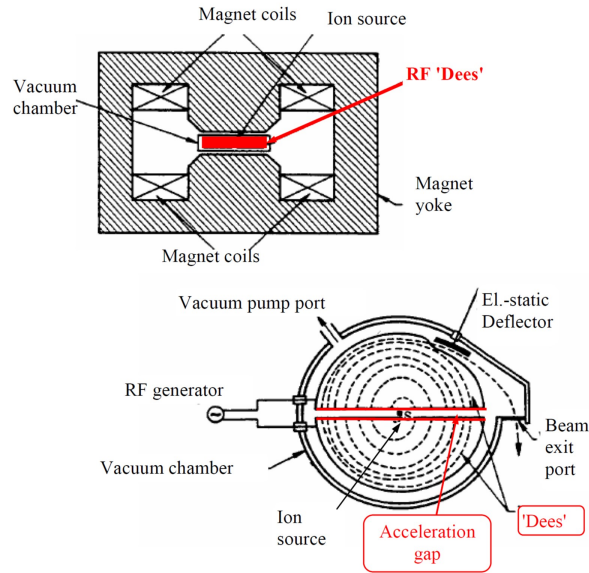
Figure 1.2: The schematic view of the cyclotron [1].

in the next round because the particle A runs a smaller trajectory than that of the particle O. In contrast, the particle B is accelerated with a higher electric field than the particle O. The particle B reaches a point B' closer to the synchronous point O' in the next round because the particle B runs a larger trajectory than that of the particle O. The field B increases and synchronizes the field B following the increase of the beam energy. We can accelerate the charged particles to a relativistic speed using synchrotrons.
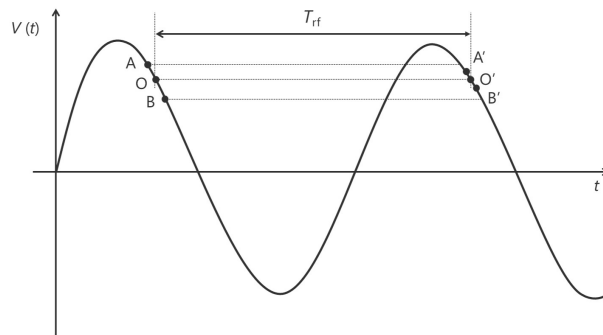
Figure 1.3: The phase stability.

The early synchrotron experiments were conducted using the Cosmotron at the Brookhaven national laboratory (BNL) and the Bevatron at the Lawrence Berkeley National Laboratory (LBNL). The Cosmotron is the first synchrotron that could accelerate protons to energies of the GeV range, in detail 3.3 GeV, starting in 1953. The Bevatron, which could accelerate protons to energies of 6.2 GeV, at LBNL had started in 1954. A lot of hadrons were discovered by the experiments with them in the 1950s and 1960s. Heavy hadrons, which were initially called V-particles and known in cosmic-ray experiments, were produced and a strangeness particle was confirmed experimentally associated with the theoretical prediction at the Cosmotron. A positron was already known as the antiparticle of an electron. Antiproton and

10

antineutron were discovered in 1955 and 1956 at the Bevalac. The facts represented that all particle has a corresponding anti-particle. $\mathcal{O}(100)$ species of hadrons discovered at the Cosmotron and the Bevatron indicated that hadrons are not elementary, but composite particles of sub-particles.

In addition to the synchrotron development, the new detector technology had also progressed particle physics. The new detector was a bubble chamber developed by Glaser in 1952. The previous experiments employed cloud chambers. Synchrotrons provided higher energies than cyclotrons. Hence, high-energy particles did not interact with the gases of cloud chambers because a gas density is too low to detect high-energy particles. He employed liquids instead of gases for the bubble chamber. A liquid density is around 1000 times larger than that of gases, therefore, the bubble chamber enabled to detect high-energy particles and to study interactions including a lot of secondary particles.

1.1.2 Quark model and the standard model

The essential progress of theories was made from the mid-1950s to the early 1960s. Kazuhiko Nishijima and Murray Gell-Mann proposed a new quantum number *strangeness* (S) independently to understand the properties of V-particles. Strangeness is defined as that it conserves in strong interactions but does not in weak interactions. Also, they introduced the hypercharge, Y, in the following formula

$$Q = I_3 + (B+S)/2 \equiv I_3 + Y/2 \tag{1.5}$$

where Q is an electric charge (proton charge is unity); I_3 is the third component of isospin, which was introduced to classify a proton and a neutron; B is a baryon number ($B = 0$: mesons, $B = 1$: baryons, and $B = 1$, $S \neq 0$: hyperons). All hadrons satisfy the Nishijima-Gell-Mann formula. Ikeda, Ohnuki, and Ogawa introduced $SU(3)$ symmetry based on the Sakata model, of which the basic particles are proton, neutron, and Λ which has a strangeness. In 1964, Gell-Mann and Zweig proposed the quark model independently to classify the experimentally discovered hadrons. The quark model is based on the $SU(3)$ group and employs three elementary particles, named *quarks*: up (u), down (d), and strange (s) quarks. $SU(3)$ is the set of unitary matrices of 3×3 with det $U = 1$. The basic expression of $SU(3)$ is a triplet. Eight independent basic vectors make the meson octet. The spin 1/2 baryon octet can be written using I_3 and Y of quarks as shown in the left panel of Fig. 1.4. The $SU(3)$ derives baryons candidates, which are combinations of qqq as shown in the right panel of Fig. 1.4. The baryons (Δ, Σ, and Ξ) were already known in the experimental results. However, the last particle in the spin 3/2 baryons composed of sss, namely Ω, was not discovered yet.

Around the same time, there was a technical improvement of synchrotrons to increase beam intensity. A beam must be focused around an ideal trajectory. The focusing technique is required at an injection of a beam to an accelerator and extraction of a beam from an accelerator. Livingston *et al.* invented the alternating-gradient focusing which is also called strong focusing. Quadrupole magnets are employed for focusing as shown in Fig. 1.5. A quadrupole magnet focuses a beam in one direction, *e.g.* the horizontal direction in the figure. The beam is diffused perpendicularly to the focusing direction (the vertical direction). Two 90 degrees rotated magnets are located on opposite sides of the magnet and they can focus the beam in both directions.

The alternating gradient synchrotron (AGS), which employs the strong focusing as its name implies, was developed at BNL. The experiment discovered a new particle using the
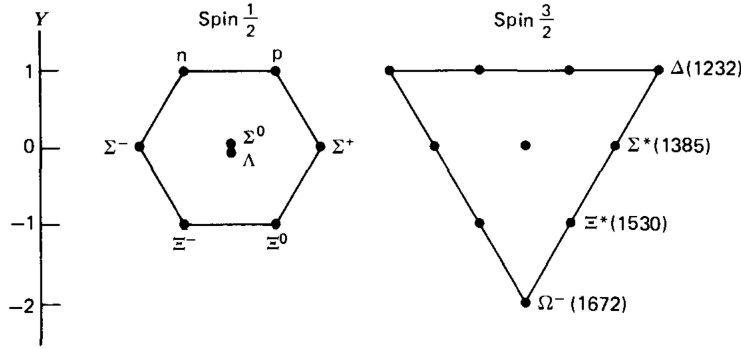
Figure 1.4: The spin 1/2 baryon octet (left) and the spin 3/2 baryon decuplet (right) [2].
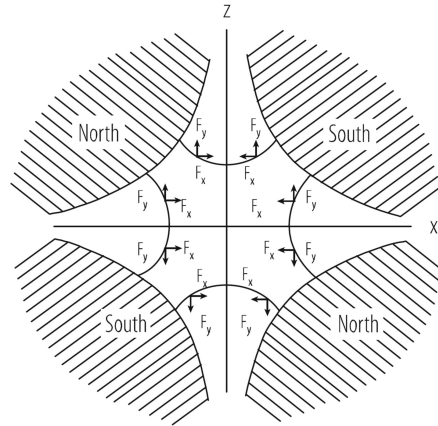
Figure 1.5: The schematic view of a quadrupole magnet [3].

AGS and a bubble chamber [4]. The properties of charge Q, strangeness S, and mass M of the new particle were $Q = -1$, $S = -3$, and $M = 1686 \pm 12 \, \text{MeV}/c^2$, respectively. They are consistent with the theoretical predictions of Ω baryon. The fact showed that the quark model was a reasonable theory.

The other valuable experimental result was also discovered in 1964; it was CP violation. Cronin and Fitch discovered CP violation via neutral K meson decays using the AGS at BNL. C is charge conjugation which means particle-antiparticle transformation. P is parity operation which means spatial reflective symmetry. Both K^0 and its antiparticle $\overline{K^0}$ have decay channels with two pions and three pions. A two-pion ($\pi^0\pi^0$) system has positive parity and a three-pion ($\pi^+\pi^-\pi^0$) system has negative parity. Therefore, a transition between K^0 and $\overline{K^0}$ are allowed via pions in a weak interaction $K^0 \leftrightarrow \{2\pi, 3\pi\} \leftrightarrow \overline{K^0}$. It is called mixing. Neutral kaons are produced in reactions such as $p + n \rightarrow p + \Lambda^0 + K^0$. The produced kaons are short-lived kaons, K_S^0, and long-lived kaons, K_L^0. K_S^0 decays into two pions and K_L^0 decays into three pions. In this case, CP is conserved. However, the decay channel of $K_L^0 \rightarrow \pi^0\pi^0$ was observed in a small probability and in that case, CP is violated.

The mixing is explained via the Cabibbo angle, θ_C, introduced by Cabibbo to understand strange particle decays in weak interactions in 1963. We consider quark bindings of the

quark state as follows

$$\begin{pmatrix} u \\ d' \end{pmatrix}, \begin{pmatrix} c \\ s' \end{pmatrix} \cdots, \tag{1.6}$$

where,

$$d' = d \cos \theta_C + s \sin \theta_C, \tag{1.7}$$

$$s' = s \cos \theta_C - d \sin \theta_C. \tag{1.8}$$

These equations are written in a matrix

$$\begin{pmatrix} d' \\ s' \end{pmatrix} = \begin{pmatrix} \cos \theta_C & \sin \theta_C \\ -\sin \theta_C & \cos \theta_C \end{pmatrix} \begin{pmatrix} d \\ s \end{pmatrix} \tag{1.9}$$

His idea was extended to three generations by M. Kobayashi and T. Masukawa. The extended matrix is called Cabbibo-Kobayashi-Masukawa matrix (CKM matrix), V_{CKM}:

$$\begin{pmatrix} d' \\ s' \\ b' \end{pmatrix} = V_{CKM} \begin{pmatrix} d \\ s \\ b \end{pmatrix} = \begin{pmatrix} V_{ud} & V_{us} & V_{ub} \\ V_{cd} & V_{cs} & V_{cb} \\ V_{td} & V_{ts} & V_{tb} \end{pmatrix} \begin{pmatrix} d \\ s \\ b \end{pmatrix} \tag{1.10}$$

where $V_{q_i q_j}$ is a squared root of a probability of a transition from quark q_j to quark q_j. The CKM matrix is unitary and the components are correlated. The CKM matrix has four independent parameters which are three real angles and an imaginary phase. The imaginary phase causes the *CP* violation. *CP* violation was measured in neutral *B* meson by the Belle experiment at KEK and by the BaBar at SLAC, respectively. Currently, LHCb at CERN and the Belle II experiment at KEK study more precisely the *CP* violation via *B* meson and also *D* meson decay channels. This physics will be described in Sec. 2.1.

The CKM matrix requires six quarks in three generations. Three out of six are new quarks: charm (*c*), bottom (*b*), and top (*t*) quarks. If the quarks were discovered, the CKM matrix is established.

J/ψ, which is composed of *c* and *c̄* quarks, was discovered by the SPEAR experiment at SLAC using the electron-positron collider accelerated energies of around 4 GeV ($\sqrt{s} = 8$ GeV) and the experiment at BNL using AGS in collisions of 28 GeV protons on a beryllium target ($\sqrt{s} \sim 5.3$ GeV) in 1974. It meant the discovery of a new quark flavor. The experiment at SLAC also discovered an excited state of charmonium, *ψ′*. The discovery is called as the *November revolution*. The discovery of the *c* quark showed the validity of the quark model and the CKM matrix. Furthermore, the E288 experiment at Fermilab discovered the bottom quark via Upsilon (Υ) meson decays in 1977 using injecting protons with the energy of 400 GeV to Cu and Pt targets ($\sqrt{s} \sim 20$ GeV) [7]. It was the first quark in the third generation. The quark model and the CKM matrix became the basis of the standard model because of the new quark discoveries.

In the 1960s, attempts had been made to uniform electromagnetic and weak interactions in parallel with the theoretical construction of the quark model. Weak interaction was proposed by E. Fermi in 1935 to describe a *beta* decay process. H. Yukawa introduced π meson as a propagator of weak interaction at the same time. His attempt proved abortive, however, the thought of exchange particles for fundamental interactions has become basic of

the standard model. Heavy particles $W^\pm$, which must have a spin of 1, were introduced as exchange particles of weak interaction. Thereafter, a neutral particle Z^0 was employed to explain neutral reactions by weak interaction. S. Glashow proposed $SU(2)_\mathrm{L} \times U(1)_Y$ for unification quantum electrodynamics and weak interaction in 1961. The additional character L explains that weak isospin current interacts with left handed Fermions. S. Weinberg and A. Salam expanded independently his idea to derive a Lagrangian which are $SU(1) \times U(1)$ invariant. The theory proposed by Weinberg and Salam unifies electromagnetic interaction and weak interaction; they are integrated electroweak interaction. The theory is called the Glashow-Weinberg-Salam (GWS) theory. The new technologies for accelerators were necessary to discover weak bosons.

Here, two types of accelerator experiments must be marshaled. In fixed-target experiments, accelerated particles are projected onto a target. The target particle momentum is zero ($\boldsymbol{p}_2 = 0$) and the projectile and target particle masses are sufficiently smaller than the projectile particle energy (m_1, $m_2 \ll E_1$), then, the center-of-mass energy in the fixed-target experiments using Eq. 1.1 can be written as:

$$\sqrt{s} = \sqrt{(E_1 + m_2 c^2)^2 - (\boldsymbol{p}_1 c)^2} \sim \sqrt{2E_1 m_2 c^2}. \tag{1.11}$$

The other important parameter is luminosity. The luminosity $\mathscr{L}$ in the fixed-target experiments are defined

$$\mathscr{L} = N_\mathrm{in} \rho l N_\mathrm{A}. \tag{1.12}$$

Here, N_in is the number of projectile particles (in /sec), ρ is the density of a target (in g/cm^3), l is the length of the target (cm), and N_A is the Avogadro constant.

In collider experiments, momenta of a projectile particle and a target particle are the same ($\boldsymbol{p}_1 = \boldsymbol{p}_2$), therefore, the center-of-mass energy in the collider experiments is the same as the sum of beam energy $\sqrt{s} = E_1 + E_2$. Thust, colliders can produce larger center-of-mass energies than fixed-target experiments effectively. The luminosity of the collider experiments is written

$$\mathscr{L} = \frac{N_1 N_2 f}{n_\mathrm{b} A} \tag{1.13}$$

where N_1 and N_2 are the numbers of particles in beamlines of an accelerator, f is rotation frequency, n_b is the number of bunches, and A is the beam area at a collision point. A is defined as $A = \sqrt{\epsilon_x \beta_x} \sqrt{\epsilon_y \beta_y}$ by amplitudes β and emittance ϵ in the perpendicular coordinate, x and y, to a beam axis z. The luminosities provided by colliders are lower than those provided the fixed-target experiments.

C. Rubbia proposed a proton-antiproton collider, a modification of the SPS, to search for the weak bosons. The significant improvement to realize a proton-antiproton collider was brought by S. van der Meer. He invented a new method to increase the luminosity of antiproton beams in a phase-space, and the method is called stochastic cooling. In a proton-antiproton collider, antiprotons are produced by projecting protons to a target. An antiproton production rate per projecting proton is 10^{-6} and around 10^{11} antiprotons are produced in a day. Antiprotons are stored in an antiproton accumulator. Stored antiprotons are not appropriate to be accelerated because they have a disordered momentum distribution which is analogous to the high-temperature antiprotons. He achieved the *cooling* and the acceleration of antiprotons by stochastic cooling. The technology enabled them to realize the super

proton-antiproton synchrotron (Sp$\bar{p}$S) at CERN. It was the world's first proton-antiproton collider. The experiments led by C. Rubbia discovered the weak bosons using the Sp$\bar{p}$S in 1983. C. Rubbia and S. van der Meer received the Nobel prize in physics. This is a good example that the new technology progresses physics. Collider experiments have become mainstream in high-energy particle physics since then.

The last quark, namely top quark, was discovered by the experiments, CDF and D0, using the proton collider, Tevatron, at the energy of $\sqrt{s} = 1.96$ TeV at Fermilab in 1995. The large hadron collider (LHC) has started in 2008 in pp collisions at $\sqrt{s} = 8$ TeV. ATLAS and CMS discovered the Higgs boson, which was the last piece of the standard model particles, in 2012. Further study for the next physics has been performed at the LHC. They are expressed in Sec. 2.1.

1.1.3 Heavy-ion physics

Strong interaction between quarks is described by quantum chromodynamics (QCD). QCD requires a gluon which propagates strong interaction. Partons, namely quarks and gluons, have color charges: red, blue, green, and their anti-colors. Combinations of quarks must be colorless, such as red+green+blue and red+anti-red. Strong interaction strength between two quarks is in inverse proportion to a distance between the quarks. It is called *asymptotic freedom*. Strength of strong interaction becomes zero in a high-energy limit and partons behave as free particles.

Heavy-ion, which is heavier nuclei than a proton, accelerators are powerful tools to test QCD in high-energy limits. Heavy-ions, such as Ne and Ar, had been accelerated to energies of 2.1 GeV/A (Ne) and 1.9 GeV/A (Ar) by the Bevalac at LBNL for the first time to search for the theoretically predicted phenomena, *e.g.* compressed hadronic matter, from 1971. It is the first heavy-ion accelerator with fixed targets. The QCD calculations predicted a hardon deconfinement phase and suggested higher center-of-mass energy, $\sqrt{s}$, of the Bevalac. The AGS at BNL has accelerated Au ion at $\sqrt{s} = 5$ GeV to search the deconfinement phase from 1986. At the same time, SPS at CERN has accelerated Pb ions at $\sqrt{s} = 17$ GeV. The experiments with SPS reported several results which imply the creation of a QGP. However, the results were inconclusive evidence for the creation of a QGP because hadron-cascade calculations can reproduce the results in a situation without a QGP. From 2000, relativistic heavy ion collider (RHIC) at BNL has started and accelerated Au ions to 100 GeV/A ($\sqrt{s_{NN}} = 200$ GeV) to produce a QGP and study the properties of a QGP. The experiments, PHENIX and STAR, reported the multiple evidence suggesting the creation of the deconfinement phase. The QGP study has been performed using the LHC at CERN. The LHC can accelerate Pb ions to the energy of 2.51 TeV ($\sqrt{s_{NN}} = 5.02$ TeV). In such energy, the properties of a QGP produced by the LHC are higher-temperature and -density than that of a QGP by RHIC. Today, researches for the understanding of the QGP properties are performed using the LHC and RHIC. The detailed physics in the heavy-ion experiments is described in Sec. 2.2.

1.2 Large hadron collider

The large hadron collider (LHC) [8] is the largest hadron accelerator of the European organization for nuclear research (CERN) and is located across the border between Switzerland and France. Figure 1.6 shows the CERN accelerator complex. Accelerators from a linear ac-

celerator (LINAC) to the super proton synchrotron (SPS) are used as boosters. A ring colored by dark blue is the LHC and it is the last ring in the accelerator chain.
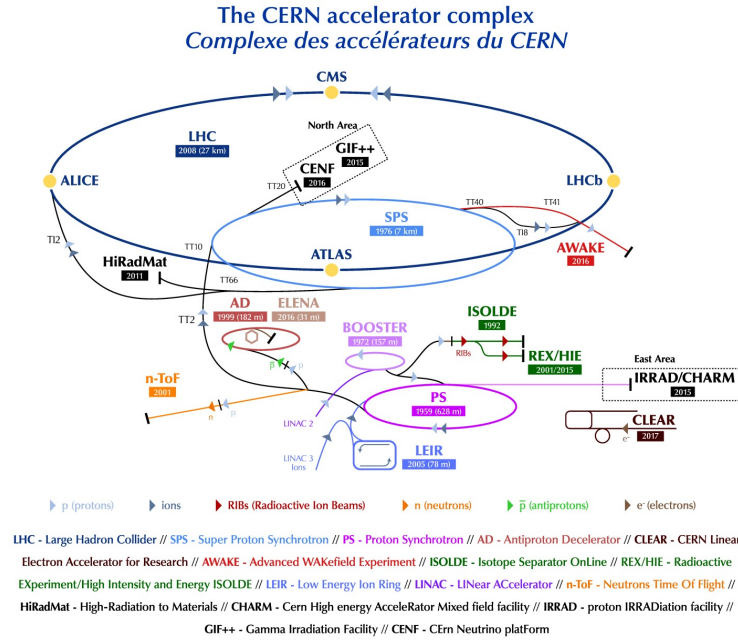
Figure 1.6: The CERN accelerator complex [9].

The center-of-mass energy of the LHC nominal design is 14 TeV in *pp* collisions and 5.5 TeV in Pb-Pb collisions. The LHC provided *pp* collisions at $\sqrt{s}$ = 8 TeV, *p*-Pb collisions at $\sqrt{s_{NN}}$ = 5.02 TeV, and Pb-Pb collisions at $\sqrt{s_{NN}}$ = 2.75 TeV in Run 1 (2009-2013). In Run 2 (2015-2018), the center-of-mass energies provided by the LHC were $\sqrt{s}$ = 13 TeV in *pp* collisions, $\sqrt{s_{NN}}$ = 8 TeV in *p*-Pb collisions, and $\sqrt{s_{NN}}$ = 5.02 TeV in Pb-Pb collisions. The peak luminosities of $\mathscr{L}_{peak} = 2 \times 10^{34}$ cm^{-2}s^{-1} for *pp* collisions was achieved at ATLAS and CMS in 2018 due to the bunch space reduction from 50 ns to 25 ns, small emittances, and smaller $\beta*$ of 30 cm than the design value of 50 cm [10]. The peak luminosity is two times larger than the design luminosity value. The designed luminosity value of $\mathscr{L}_{peak} = 1 \times 10^{27}$ cm^{-2}s^{-1} for Pb-Pb collisions was achieved at ALICE in Run 2. The peak luminosity for Pb-Pb collisions will be $\mathscr{L}_{peak} = 6.4 \times 10^{27}$ cm^{-2}s^{-1} at ALICE in Run 3 (2022-2024) thanks to an increase of a collision rate to 50 kHz [10].

1.2.1 HL-LHC

The center-of-mass energy of 14 TeV provided by the LHC will be the highest at least in the next decade since we need a larger circular collider than the LHC to generate a larger center-of-mass energy than that of the LHC. However, an increase of luminosity can be achieved. CERN upgrades the LHC luminosity above the nominal design in the 2020s and the name is the high-luminosity LHC (HL-LHC) [10]. The Run 3 term is the transition stage from the LHC to the HL-LHC. The innovative technologies are employed for the HL-LHC, *e.g.* 11 to 12 T superconducting magnets, RF cavities for beam rotation with ultra-precise phase control, new technologies, and material for beam collimation, and high-current supercon-

ducting links with almost zero energy dissipation. The technologies will provide focused beams, that reduce a beam cross-sectional area A in Eq. 1.13.

The peak luminosity of the HL-LHC will be reached $\mathscr{L}_{\text{peak}} = 5 \times 10^{34}$ cm^{-2}s^{-1} in Run 4 starting in 2028 with a bunch crossing rate of 40 MHz (ultimately $\mathscr{L}_{\text{peak}} = 7.5 \times 10^{34}$ cm^{-2}s^{-1} in Run 5) for pp collisions as shown in Fig. 1.7. The HL-LHC will provide more data than the whole LHC data and the data will enable us to observe rare processes and new phenomena. In such high-luminosity levels, the number of concurrent proton-proton interactions, which are called pileup events, per bunch crossing reaches as many as 200.
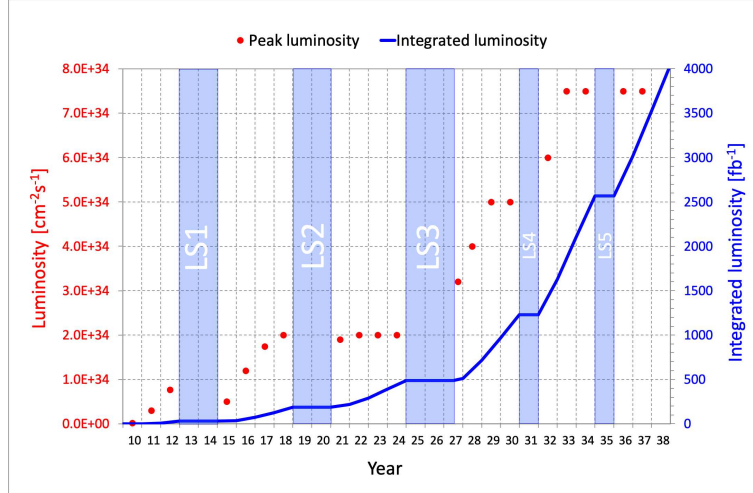
Figure 1.7: The ultimate HL-LHC peak luminosity (red dots) and integrated luminosity (blue line) for pp collisions [11].

1.3 Electron-positron collider

Electron-positron colliders, such as the superKEKB, produce less background compared to hadron colliders. Less background allows recording pure physics signals. The current electron-positron colliders are circular colliders. Electrons and positrons lose their energies due to bremsstrahlung. The cross-section of bremsstrahlung is $\sigma_{br} \propto Z^2 \alpha^3 / m_e^2 c^4$. In the case of heavier particles than electrons and positrons, the effect of bremsstrahlung can be ignored. Therefore, an acceleration efficiency of a synchrotron electron-positron collider is not as high as that of a hadron collider. The hadron colliders or a linear accelerator, such as the international linear collider (ILC), are necessary for physics researches in the high-energy frontier.

1.4 Scope of this thesis

As described, particle physics has progressed with the evolution of experimental technologies. Even today, innovations of technologies impact on the particle physics. The LHC upgrades will be able to progress the particle physics. At the LHC, the increase of luminosity is the main upgrade project by higher collision rates or small cross-sectional areas of beams. A

data volume will grow with the increase of luminosity. Hence, data acquisition systems will encourage particle physics to process data.

In this thesis, technologies of the data acquisition and processing systems will be described and physics impacts provided by the technologies will be discussed at large-scale hadron collider experiments in the higher-luminosity era.

Chapter 2

Physics at the LHC

In this section, the research topics at the LHC, the standard model, and beyond the standard model are written in 2.1, and the heavy-ion physics is shown in 2.2.

2.1 Standard model and beyond

All the standard model particles were founded due to the discovery of a Higgs particle in 2012. Properties of a Higgs boson are measured precisely.

2.1.1 Higgs boson

P. Higgs proposed a model to explain masses of weak bosons in 1964. The model is called the Higgs mechanism and needs a new boson which is a spin-parity of 0+ and named a Higgs boson. Search for a Higgs boson was a high-priority issue of the LHC that started in 2009. ATLAS and CMS reported discoveries of a new boson, whose mass and spin-parity are 125 GeV/c^2 and 0+, individually in 2012. The parameters were consistent with the prediction and the fact showed the new boson is a Higgs boson. The research phase has moved from the search for a Higgs boson to the study of a Higgs boson. Precise measurements of the coupling to other particles and to itself are necessary to understand the Higgs mechanism.

Measurements of coupling strength of a Higgs boson to other particles are evaluated using combinations of a production process and a Higgs decay channel. Four main processes are predicted in the standard model and their Feynman diagrams are shown in Fig. 2.1. The gluon gluon fusion (ggF) produces only a Higgs boson. Decay objects of a Higgs boson are detected. The vector boson fusion (VBF) produces a Higgs boson and a pair of quarks and each quark is detected as a jet which is a bunch of high-energy hadrons. The vector boson associated production (VH) produces a weak boson, W/Z, in addition to a Higgs boson. Weak bosons have decay channels of $Z \rightarrow \nu\nu$, $W \rightarrow \nu\ell$, and $Z \rightarrow \ell\ell$. These decay modes are triggered easily because their decay objects have large-p_T or large missing energy $E_\mathrm{T}^{\mathrm{miss}}$. The top quark pair associated production (ttH) is a direct probe of a top quark and a Higgs boson coupling. A top quark decays to a bottom quark and a W boson mainly. Thus, the ttH production is detected via a b-jet and W decay products.

The standard model also predicts decay channels of a Higgs boson. Table 2.1 shows the branching ratios and the relative uncertainty of the Higgs decay channels. The Higgs decaying to a pair of b-quarks, $H \rightarrow b\bar{b}$, is the dominant channel in the Higgs decay channel.

gluon-gluon fusion (ggF)

vector boson fusion (VBF)

vector boson associated production (VH)   top quark pair associated production (ttH)
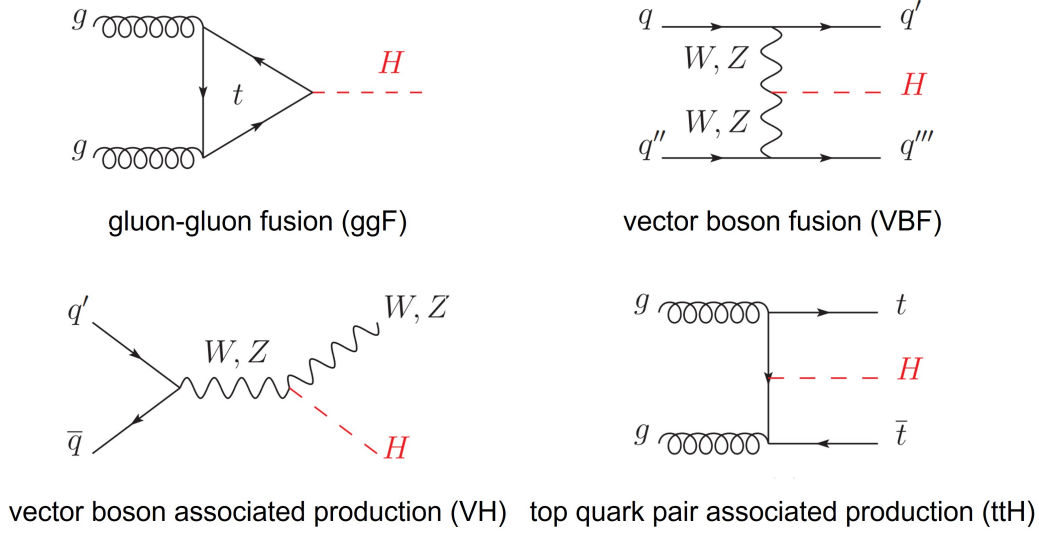
Figure 2.1: The Feynman diagrams of Higgs production from Ref. [12].

Each b-quark is observed as a jet, therefore, a *tagging* of the jet is needed. The weak boson decay channels of a Higgs boson are measured via the weak boson decay channels. The two tau decay channel is measured via jets because 64 % of taus decay to hadrons. Therefore, a dedicated trigger for tau leptons is necessary to identify tau decay jets and other jets. The channel $H \to c\bar{c}$ is not observed.

Table 2.1: The branching ratios and the relative uncertainty for a Higgs boson with $m_H = 125$ GeV [12].

Decay channel	Branching ratio	Rel. uncertainty
$H \to \gamma\gamma$	2.27×10^{-3}	2.1%
$H \to ZZ$	2.63×10^{-2}	$\pm 1.5\%$
$H \to W^+W^-$	2.14×10^{-1}	$\pm 1.5\%$
$H \to \tau^+\tau^-$	6.27×10^{-2}	$\pm 1.6\%$
$H \to b\bar{b}$	5.82×10^{-1}	$+1.2\%$ -1.3%
$H \to c\bar{c}$	2.89×10^{-2}	$+5.5\%$ -2.0%
$H \to Z\gamma$	1.53×10^{-3}	$\pm 5.8\%$
$H \to \mu^+\mu^-$	2.18×10^{-4}	$\pm 1.7\%$

The measurements of the coupling strength were performed by ATLAS and CMS. Figure 2.2 shows the mass-dependent coupling strength measured by ATLAS in Run 2 [13]. The blue dotted line is the mass-dependent coupling strength evaluated by the standard model. The black points are measured strength experimentally. The bottom panel shows the normalized by the calculation. The measured strength to a top and weak bosons are consistent with the standard model with uncertainties of less than 10 %. The couplings to a bottom and a tau are corresponding to the standard model with errors of 15 %. The coupling to a muon is in agreement with the calculation with errors of 30 %. The confidence level of the coupling is 95 % and more amount of statistics are necessary to test the standard model. It is

20

difficult to measure the coupling to an electron even at the HL-LHC [63]. If there is a differ-ence between a measured strength and the standard model prediction, it will be a signature of new physics, because the couplings of Higgs bosons to other particles generate masses of the particles and the difference needs a mass generation via another Higgs boson which is predicted in beyond the standard model.
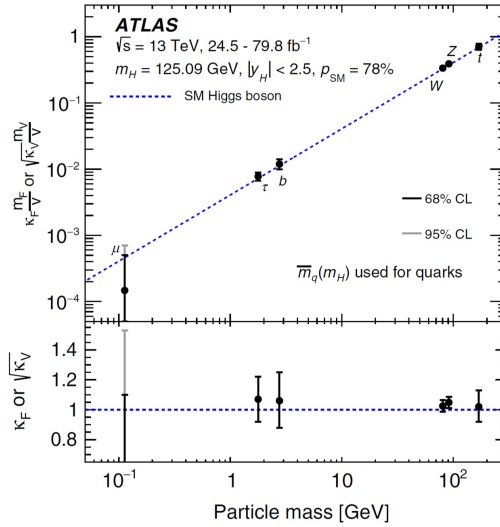
Figure 2.2: The interaction strength of Higgs and other particles [13].

In addition, the self-coupling of a Higgs boson is an important parameter to understand the Higgs mechanism because its potential can be determined experimentally via the self-coupling. Measurements of self-coupling strength are performed via pair productions of Higgs bosons. The main production processes are shown in Fig. 2.3. The cross-section of di-Higgs boson productions is around one-thousandth of the cross-section of the single Higgs production processes. Figure 2.4 shows the upper limits of the pair Higgs productions in each decay channel in a 95 % confidence level at ATLAS in Run 2.

Figure 2.3: The Feynman diagrams of a Higgs boson pair [12].

2.1.2 CP violation

CP violation measurements provide the standard model test with a different perspective than the Higgs measurements. *CP* violation in *B* meson decays was discovered by the Belle
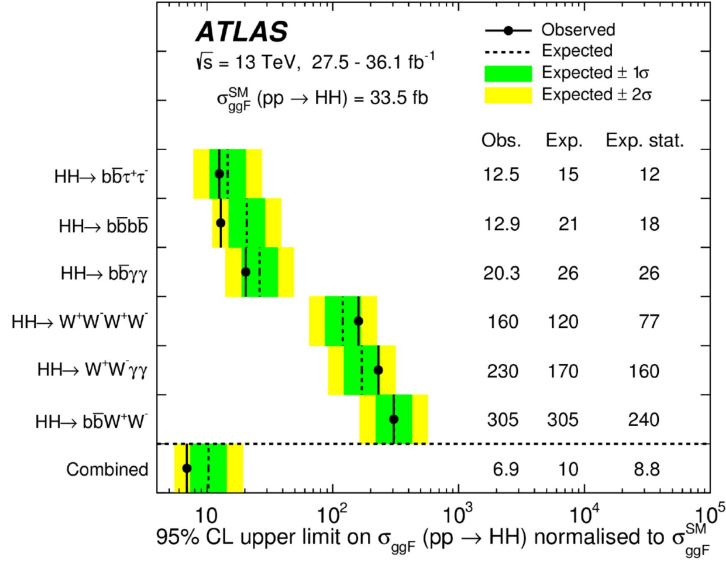
Figure 2.4: The upper limits of the pair production cross-section [14].

experiment at KEK and by the BaBar experiment at SLAC in 2001. In 2019, *CP* violation in the *D* meson decays was discovered at LHC. *CP* violation measurements in heavy quark meson systems are powerful ways to test the standard model.

The CKM matrix mentioned in Sec. 1.1 explains the mixing of mesons. The CKM matrix is unitary. Test for a unitary triangle, which is provided by the CKM matrix, is equal to test for the CKM matrix. The unitarity of the CKM matrix described in Eq. 1.10 leads to six relations of the matrix elements. For example, the triangle in a B^0 (bd) is written as

$$V_{ud}V_{ub}^* + V_{cd}V_{cb}^* + V_{td}V_{tb}^* = 0 \tag{2.1}$$

and the triangle in a D^0 (cu) is described as

$$V_{ud}V_{cd}^* + V_{us}V_{cs}^* + V_{ub}V_{cb}^* = 0. \tag{2.2}$$

The B^0 triangle is drawn in the complex plane as shown in Fig. 2.5 using the unitarity as Eq. 2.1. Here, Eq. 2.1 is normalized as follows:

$$\frac{V_{ud}V_{ub}^*}{V_{cd}V_{cb}^*} + \frac{V_{td}V_{tb}^*}{V_{cd}V_{cb}^*} + 1 = 0. \tag{2.3}$$

The parameters, $\bar{\rho}$ and $\bar{\eta}$, in the B^0 triangle are given by

$$\bar{\rho} + i\bar{\eta} = -\frac{V_{ud}V_{cb}^*}{V_{cd}V_{cb}^*}. \tag{2.4}$$

If the triangle is closed, the standard model is correct. If not, another contribution of new physics to *CP* violation is implied.

Parameters in Figure 2.5 are evaluated via rare decays of *B* and *D* mesons. For instance, the angle, γ, is determined via the processes, such as $B^\pm \to D^0 K^\pm$ whose branching ratio is less than 1.3×10^{-5}. The evaluated value of γ is $(74.0^{+5.0}_{-5.8})^\circ$ using the LHCb detector [16] .
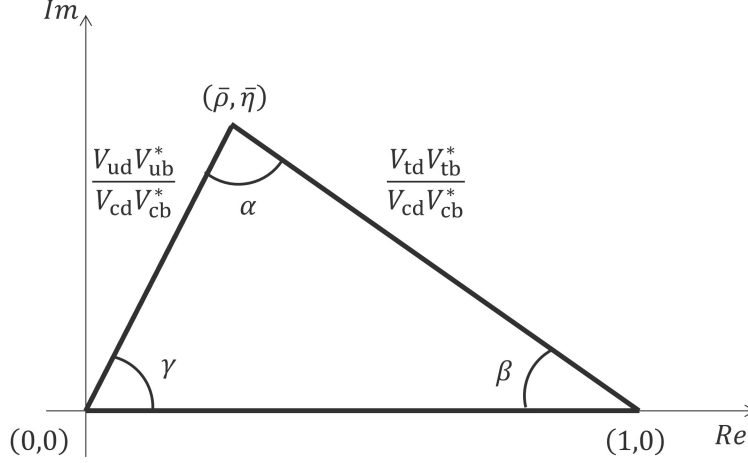
Figure 2.5: The B^0 triangle.

High-precision measurement of less than $1°$ for γ is necessary to match anticipated theory improvements [17]. Similarly, the angles (α, β, and γ) and the components of the triangle sides (V_{ub}, V_{cb}, and V_{td}) can be determined by measurements of B meson decays. D meson measurements contribute to the components of the triangle sides (V_{cd}, and V_{cs}).

B and D mesons are reconstructed by their decay products which are leptons and hadrons. Lifetimes of B mesons, $c\tau_B$, and D mesons, $c\tau_D$ are approximately 450 μm and 100 μm, respectively. They are longer than other hadrons and have secondary vertices which mean decay points of B and D mesons. Detection and tracking of all particles are crucial to the determination of secondary vertex with identified decay particles. The LHCb detector is located in the forward region, $2 < \eta < 5$, because particles are boosted in a forward direction and the detector setup has an advantage for secondary vertex measurement.

2.1.3 Supersymmetry

Supersymmetry (SUSY) is beyond the standard model. SUSY predicts super-partners for every standard model particle at the TeV scale as shown in Fig. 2.6. The masses of SUSY particles are above $\mathcal{O}(1)$ TeV/c^2. SUSY particles, suc as squarks and gluinos, are searched with a significant missing transverse energy $E_\mathrm{T}^\mathrm{miss}$ because stable SUSY particles interact very weakly with detectors.

2.2 Heavy-ion physics

2.2.1 Quark-gluon plasma

The behavior of partons, namely quarks and gluons, is described by QCD. The QCD coupling constant α_s is written as

$$\alpha_\mathrm{s} = \frac{12\pi}{(33 - 2n_\mathrm{f})\ln(Q^2/\Lambda^2)}. \tag{2.5}$$

Here, n_f is the number of flavors and Q^2 is momentum transfer. Λ shows the QCD scale parameter, which is derived from QCD calculation and experiments, and the typical value is

Names	Spin	P_R	Gauge Eigenstates	Mass Eigenstates
Higgs bosons	0	+1	$H_u^0 \ H_d^0 \ H_u^+ \ H_d^-$	$h^0 \ H^0 \ A^0 \ H^\pm$
squarks	0	-1	$\tilde{u}_L \ \tilde{u}_R \ \tilde{d}_L \ \tilde{d}_R$ $\tilde{s}_L \ \tilde{s}_R \ \tilde{c}_L \ \tilde{c}_R$ $\tilde{t}_L \ \tilde{t}_R \ \tilde{b}_L \ \tilde{b}_R$	(same) (same) $\tilde{t}_1 \ \tilde{t}_2 \ \tilde{b}_1 \ \tilde{b}_2$
sleptons	0	-1	$\tilde{e}_L \ \tilde{e}_R \ \tilde{\nu}_e$ $\tilde{\mu}_L \ \tilde{\mu}_R \ \tilde{\nu}_\mu$ $\tilde{\tau}_L \ \tilde{\tau}_R \ \tilde{\nu}_\tau$	(same) (same) $\tilde{\tau}_1 \ \tilde{\tau}_2 \ \tilde{\nu}_\tau$
neutralinos	1/2	-1	$\tilde{B}^0 \ \tilde{W}^0 \ \tilde{H}_u^0 \ \tilde{H}_d^0$	$\tilde{N}_1 \ \tilde{N}_2 \ \tilde{N}_3 \ \tilde{N}_4$
charginos	1/2	-1	$\tilde{W}^\pm \ \tilde{H}_u^+ \ \tilde{H}_d^-$	$\tilde{C}_1^\pm \ \tilde{C}_2^\pm$
gluino	1/2	-1	$\tilde{g}$	(same)
goldstino (gravitino)	1/2 (3/2)	-1	$\tilde{G}$	(same)

Figure 2.6: The list of the standard model particles and their super-partners predicted by SUSY [18].

$\Lambda \sim 250$ MeV$/c^2$. Q^2 depends on the distance between partons and becomes large when the distance becomes short. Coupling between partons becomes zero asymptotically in $Q^2 \to \infty$. It is called asymptotic freedom, which is one of the QCD nature. On the other hand, the coupling between partons is strong when the distance is large. Therefore, each parton is constrained in hadrons and it is called quark confinement.

The lattice-QCD calculation predicts that a temperature of a system becomes the critical temperature, T_c, of around 200 MeV and the energy density and the pressure of the system increase drastically due to the quark deconfinement as shown in Fig. 2.7. The quark deconfined state is called the quark-gluon plasma (QGP).
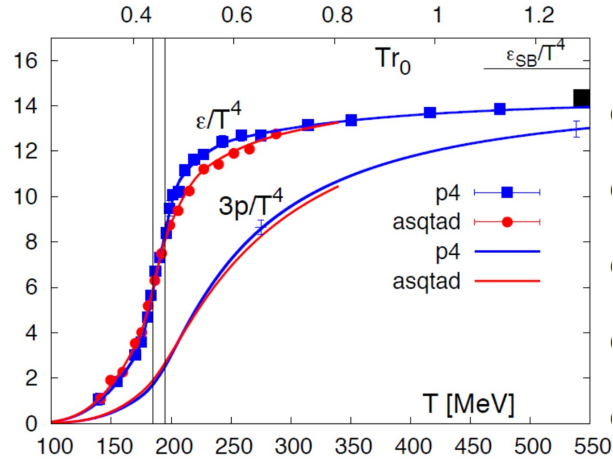
Figure 2.7: The temperature dependence of the energy density and pressure calculated using the lattice-QCD [19].

24

2.2.2 Heavy-ion collision experiment

High-energy heavy-ion collision is a powerful tool to study the QGP experimentally. A heavy-ion collision has a drastic space-time evolution including the QGP and subsequent hadronic matter. Evolution is separated into several stages.

1. Color glass condensate: Saturated state of gluons which are produced by quarks in accelerated nuclei

2. Initial collision: Partons in colliding nuclei toward each other scatterings in a reaction region

3. Glasma: Intermediate state of the color glass condensate and the QGP phase

4. QGP phase: Thermal equilibrium and partonic state with a high energy density created by parton scatterings

5. Hadronic phase: Hadronized parton state when the system expands and the temperature becomes below T_c

6. Freeze-out: No more particle production in a chemical freeze-out and then no more change of momentum in a kinetic freeze-out

Time →

| Initial | Energy Stopping | Hydrodynamic | Hadron |
| State | Hard Collisions | Evolution | Freezeout |
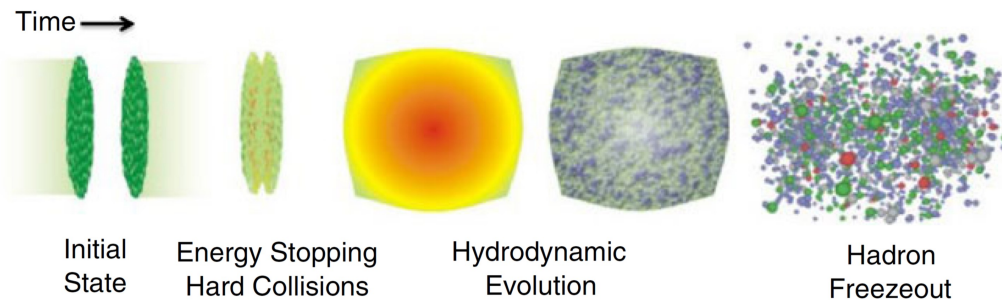
Figure 2.8: The time evolution of a heavy-ion collision [20].

Integrated particles produced in a whole history are measured. A study of each stage means understanding the whole history of a heavy-ion collision. Therefore, the comprehension of the whole history of a heavy-ion collision is crucial to study each stage using particles sensitive to each stage. It indicates that various measurements are necessary for a study of the QGP properties. Essential results are described in the next section.

2.2.3 Evidence of QGP creation

A lot of physics data were collected from 2000 at RHIC, where the QGP creation has been ensured for the first time experimentally. Then, the LHC since 2009 is the frontier of the QGP study as well as RHIC. Here, four significant results proving the QGP creation are described.

1. Jet quenching A jet is a bunch that contains a lot of high-energy hadrons. High-energy initial parton-parton scattering produces a pair of energetic partons. Then, hadrons are produced by the fragmentation of partons. If a high-density medium like the QGP is produced, partons in jets lose their energy due to interactions with the medium. Therefore, jets are quenched finally and an amount of energy loss depends on a medium density.

Figure 2.9 shows the schematic view of a jet quenching. It is illustrated that the jet passing a long-range in a matter loses more energy and is quenched relative to the jet runs a short-range inside the matter. Jet quenching is one of the most important pieces of evidence of QGP creation.
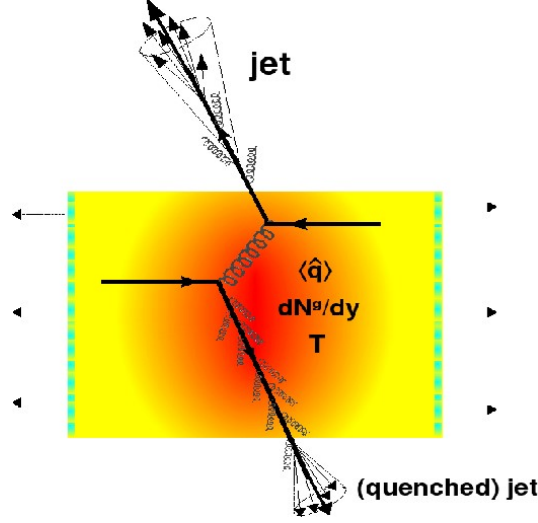
Figure 2.9: The schematics of jet quenching [21].

The nuclear modification factor, R_{AA}, is introduced to quantify results between AA and pp collisions. R_{AA} is defined as

$$R_{AA} = \frac{E\frac{d^3 N_{AA}}{dp^3}}{N_{\mathrm{coll}}E\frac{d^3 N_{pp}}{dp^3}}. \tag{2.6}$$

Here, $E\frac{d^3 N_{AA}}{dp^3}$ and $E\frac{d^3 N_{pp}}{dp^3}$ are the invariant yields in AA collisions and pp collisions, respectively. N_{coll} is the number of binary collisions in an AA collision. If R_{AA} is equal to unity, it means that a yield in AA collisions results from a superposition of pp collisions. If not, the difference is induced by a new matter.

Figure 2.10 shows the p_{T} dependent jet R_{AA} in Pb-Pb collisions at $\sqrt{s_{\mathrm{NN}}}$ = 2.76 TeV in the centrality ranges of 10-30 %, 5-10 %, and 0-5 % measured by CMS [22]. The filled circles are measured R_{AA}. The error bars mean the statistical uncertainties. The yellow boxes represent the p_{T} dependent systematic uncertainties. The gray shaded boxes are an additional systematic uncertainty from the normalization and the pp integrated luminosity. The results show that the p_{T} dependent jet yield in Pb-Pb collisions is suppressed. It suggests that jets lose their energy in the medium.

An amount of energy loss of partons, ΔE, is proportional to a parton stopping power of the matter, $\hat{q}$. The stopping power is defined as $\hat{q} = m_D^2/\lambda$. Here, m_D is a Debye mass and λ is a mean free path. Figure 2.11 shows the comparisons of experimentally measured R_{AA}
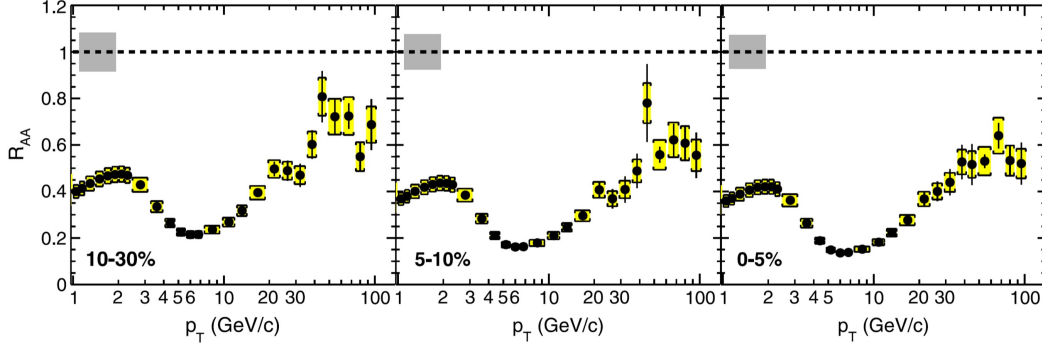
Figure 2.10: The jet R_{AA} measured by CMS in Pb-Pb collisions at $\sqrt{s_{NN}} = 2.76$ TeV [22].

and theoretical calculations. The black points and the blue stars represent the p_T dependent jet R_{AA} in the most central Pb-Pb collisions at $\sqrt{s_{NN}} = 2.76$ TeV by CMS and ALICE, respectively. The magenta dashed lines are the fit to the combined experimental data with $\hat{q} = 1.4$, 1.8, 2.6, and 3.0 GeV^2/fm from the top. The red line is the best fit for the combined experimental data. The fit leads the stopping power of $\hat{q} = 2.2 \pm 0.5$ GeV^2/fm.
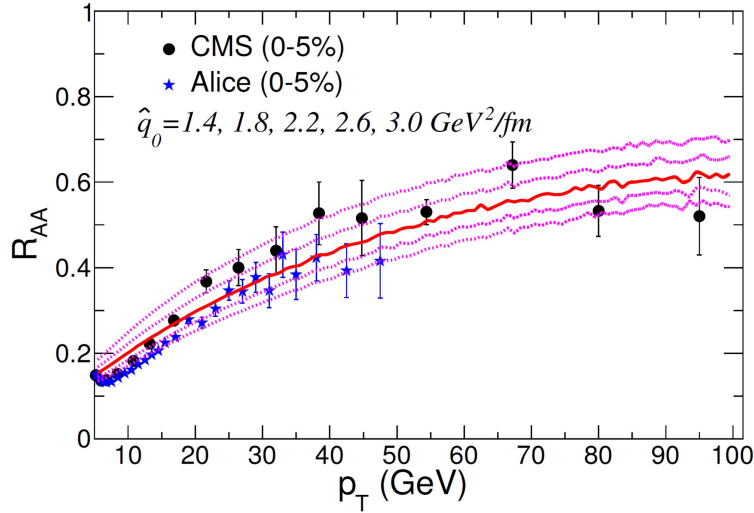
Figure 2.11: The comparisons of the experimentally measured jet R_{AA} and calculations [23].

2. J/ψ suppression J/ψ is a quarkonium composed of charm quarks ($c\bar{c}$) and is sensitive to the QGP temperature. J/ψ is produced mainly by gluon fusion in initial collisions and has a whole space-time evolution experience. Hence, we can study matter effects using J/ψ.

J/ψ melts by the Debye screening in the QGP. Quarks of J/ψ are screened by many light quarks in the QGP as shown in Fig. 2.12. The c quarks bind light quarks and then the number of J/ψ is decreased. A yield in AA collisions is suppressed compared to a superposition yield of pp collisions. This is the J/ψ suppression by the Debye screening.

According to the lattice-QCD calculation, a suppression level depends on a temperature of a QGP. Figure 2.13 shows the lattice-QCD calculations for $c\bar{c}$ spectral functions. The horizontal axis and the vertical axis represent a real frequency and the magnitude of spectra.

27
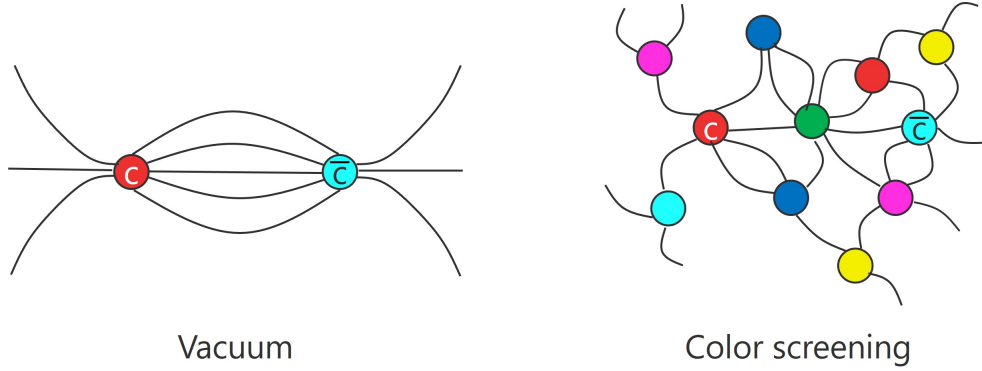
Figure 2.12: The Debye screening in a QGP.

The long dashed-dotted line, the dashed line, and the solid line in Fig 2.13 (a) represent the J/ψ spectra at the temperatures of $0.78T_\mathrm{c}$, $1.38T_\mathrm{c}$, and $1.62T_\mathrm{c}$. The solid line and the dashed line in Fig 2.13 (b) are also the J/ψ spectra at the temperatures of $1.87T_\mathrm{c}$ and $2.33T_\mathrm{c}$. The plots show that J/ψ melts in the matter temperature of $1.87T_\mathrm{c}$. Also, the J/ψ production is more suppressed in the higher temperature. The peaks in $\omega = 0$ in Fig. 2.13 (b) are calculation errors.
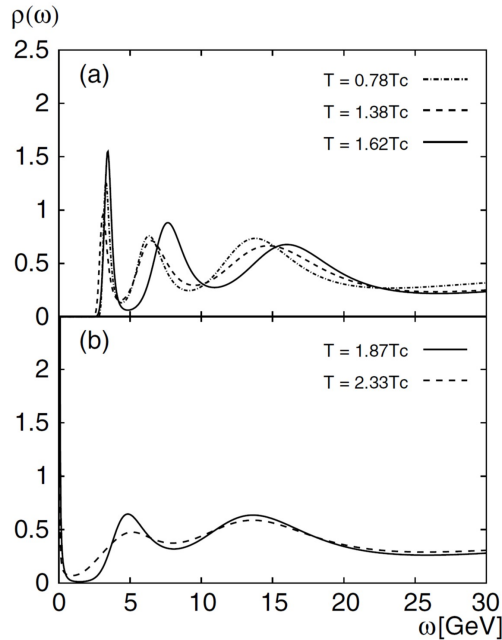
Figure 2.13: The temperature-dependent J/ψ spectra QCD calculated by lattice-QCD [24].

Figure 2.14 shows the p_T dependent J/ψ R_AA measured by ALICE with the red points and PHENIX with the black points. Both R_AA is suppressed and the figure shows the temperatures of the QGP at the LHC and RHIC are above $2T_\mathrm{c}$. In addition to this, the results present that the suppression level at the LHC is smaller than that of RHIC, especially in the low p_T region. It is thought to be due to J/ψ recombination. The recombination is that a screened c ($\bar{c}$) quark binds another screened $\bar{c}$ (c) quark because the number of $c\bar{c}$ pairs at the

28

LHC is larger than that in RHIC.
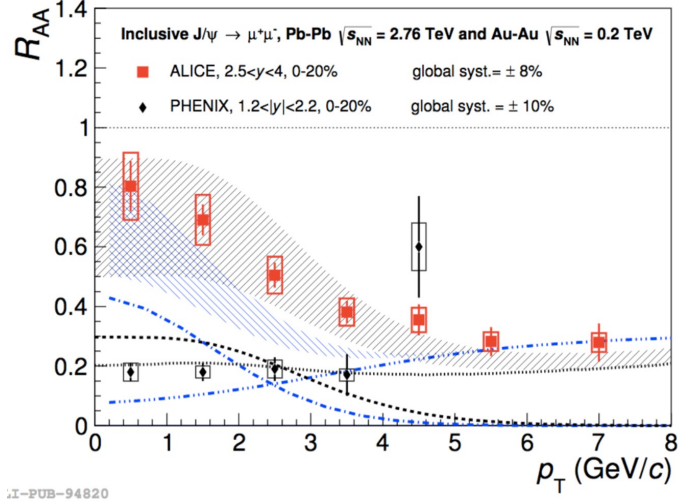
Figure 2.14: The p_T dependent J/ψ suppression measured by ALICE and PHENIX and the transport models [27].

A suppression is observed for other quarkonia, $\psi(2S)$ ($c\bar{c}$) and the Upsilon family ($b\bar{b}$). The temperatures of quarkonia melting depend on the state as shown in Tab. 2.2. The quarkonia meltings act as a thermometer of the QGP.

Table 2.2: The dissociating temperature of quarkonia [26] .

State	χ_c	ψ'	J/ψ	Υ'	χ_b	Υ
T_dis	$\leq T_c$	$\leq T_c$	$1.2T_c$	$1.2T_c$	$1.3T_c$	$2T_c$

3. Elliptic flow An elliptic flow is a corrective motion of particles. The flow is caused by a high-density matter expansion due to its intrinsic pressure. Figure 2.15 shows the schematic view of an elliptic flow. A shape of a reaction region is rugby-ball shaped when a collision is non-central. A high-dense matter having initial spatial anisotropy is produced in the reaction region. Spatial anisotropy is made by a shape of a reaction region. A pressure gradient of the dense matter in the direction of a reaction plane (the $x - z$ plane) is larger than a gradient in the y-direction. Finally, particles in the matter move and expand in the direction of the pressure gradient as fluid. It means that momentum anisotropy is produced because particles are received momentum kick in the direction of the $x-z$ plane by a pressure gradient.

The anisotropy parameter v_2 is written using the azimuthal direction of particles, ϕ, as

$$\frac{dN}{d\phi} \propto 1 + 2v_2 \cos 2(\phi - \Phi_\mathrm{RP}).\tag{2.7}$$

Here, Φ_RP represents the direction of a reaction plane in a given collision. Figure 2.16 is the p_T dependent v_2 measured by PHENIX at RHIC in Au + Au collisions at $\sqrt{s_\mathrm{NN}} = 200$ GeV.

29
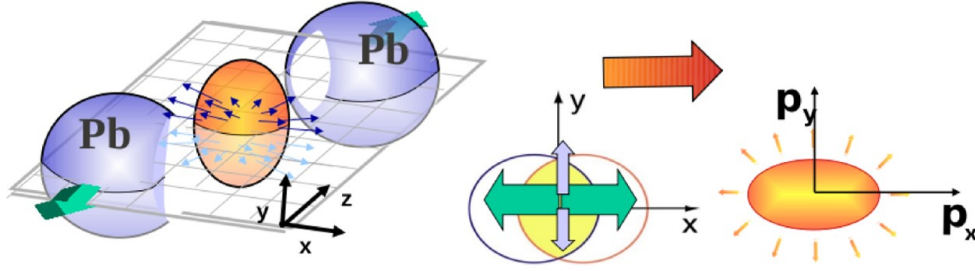
Figure 2.15: The schematics of an elliptic flow [28].

The triangles, the squares, and the circles are v_2 of $\pi^{\pm}$, $K^{\pm}$, and $p(\bar{p})$. The solid lines are relativistic hydrodynamics calculations for the elliptic flow of pions, Kaons, and protons. The hydro-dynamics calculations employ viscosity of zero and thermalization time of $\tau_0 = 0$. If viscosity is large, a fluid flow is disturbed and v_2 becomes small due to the viscosity and a calculation cannot replicate the experimental result. The comparisons of the experimental results and the calculations suggest that fluid extremely small viscosity is produced in the reaction region and becomes a thermal equilibrium state in a short time.
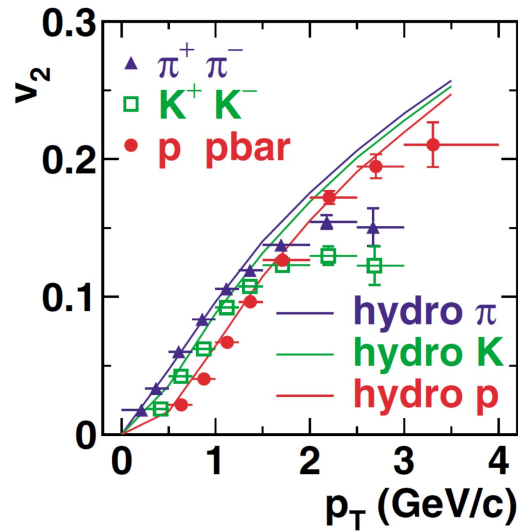
Figure 2.16: The elliptic flow of proton, pion, and Kaon measured by PHENIX [29].

4. Thermal photons   The QGP has thermal radiation because the QGP is a thermal equilibrium state. Then, a thermal photon measurement is a direct temperature measurement of the QGP. Thermal photons are components of direct photons. A direct photon is defined as a non-hadron decay photon. Other components of direct photons are prompt photons, which are produced in initial scatterings, and photons produced by hadron interactions in hadron gas. A summation of direct photon components is measured experimentally. Thermal photon is the dominant component of the direct photon in the p_T range of 1-3 GeV/c.

Figure 2.17 shows the direct photon p_T distribution at ALICE in Pb-Pb collisions at

$\sqrt{s_{\text{NN}}} = 2.76$ TeV [30]. The red circles, the green diamond shapes, and the blue cross shapes represent direct photon spectra for the centrality ranges of 0-20 % scaled by a factor 100, 20-40 % scaled by a factor 10, and 40-80 %, respectively. The solid lines and the shaded bands are next-to-leading order perturbative-QCD calculations for the direct photon yield in pp collisions scaled by the number of binary collisions for each centrality range. There are excesses in the p_{T} of 1-3 GeV/c. A fitting the Boltzmann distribution, $e^{-p_{\text{T}}/T}$, to the excess component provides an effective temperature of the QGP. The effective temperature at the LHC is evaluated as $304 \pm 11^{\text{stat}} \pm 40^{\text{sys}}$ MeV. The temperature is high enough to create the QGP.
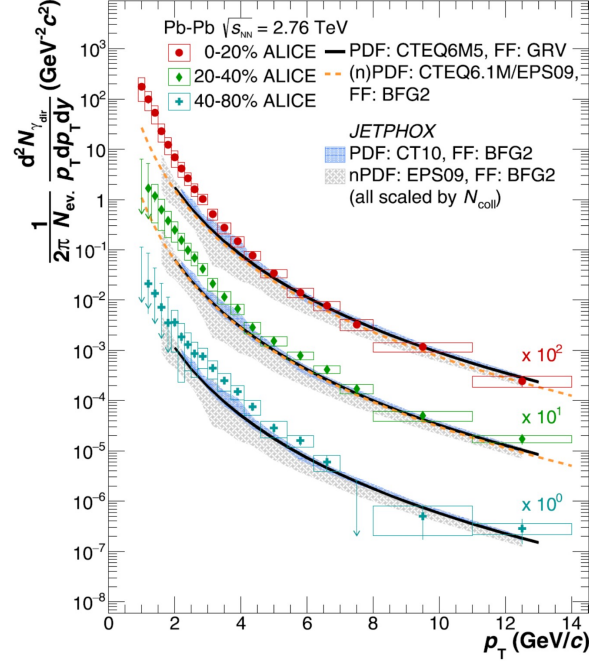
Figure 2.17: The transverse momentum distribution of direct photons at ALICE [30].

2.2.4   Future researches

The presence of a QGP has ensured the evidence as shown in Sec. 2.2.3. Our understanding of the nature of the QGP should be improved to explain the QGP and phenomena in a high-temperature matter. The research phase has been moved to high-precise measurements of the QGP property This sub-section describes the topics that must be addressed in the next experiments.

1. Heavy quarks   Heavy quarks (c and b quarks) are known as good probes for the QGP study. Their masses are $m_c \sim 1.3$ GeV/c^2 and $m_b \sim 4.8$ GeV/c^2, respectively. They are much larger than the QCD scale. Also, heavy quarks are not produced thermally because a typical temperature of the QGP is less than 1 GeV and several hundred MeV at most. Heavy quarks formation times are calculated as $t_c \sim 1/2m_c \sim 0.1$ fm/c and $t_b \sim 1/2m_b \sim 0.01$ fm/c. They are shorter than the QGP formation time 0.1-1 fm/c. Therefore, we can study the properties of the QGP using heavy quarks.

Low-p_T heavy quarks move randomly (the Brown motion) in the QGP and loss their energy due to elastic collisions between them and partons of the medium. Kinematics of a low-p_T heavy quark is described by the Langevin equation

$$\frac{d\boldsymbol{p}}{dt} = -\eta_D(p)\boldsymbol{p} + \xi \tag{2.8}$$

where η_D is friction coefficient and ξ is shaking force. The momentum diffusion coefficient, D_p, and spatial diffusion coefficient, D_s, of the medium are written as

$$D_p = m_q T \eta_D, \; D_s = T/m_q \eta_D. \tag{2.9}$$

Kinematics variation from an initial state to a final state includes information of D_p and D_s of the QGP. High-p_T heavy quarks lose their energy due to gluon radiation. Also, amounts of energy loss would decrease with increasing mass due to the dead-cone effect. It is considered that mass dependence of energy loss is $\Delta E_g > \Delta E_{u,d,s} > \Delta E_c > \Delta E_b$.

Figure 2.18 shows the D meson R_{AA} in 0-10 % central Pb-Pb collisions at $\sqrt{s_{NN}} = 5.02$ TeV at ALICE and the heavy quark transport models. The black points and the orange cross shapes represent the averaged non-strange D meson R_{AA} and the D_s^+ R_{AA}. The statistical and systematic uncertainties are described by the error bars and the boxes. PHSD, TAMU, and Catania are heavy quark transport models in the medium and coalescence. The D_s^+ R_{AA} is larger than the non-strange D meson R_{AA} for $p_T < 10$ GeV/c as the model predictions. However, the experimental uncertainties are too large to constrain the models. Therefore, precise measurements of heavy quarks are essential to estimate the property of the QGP.

ALI-PREL-320222
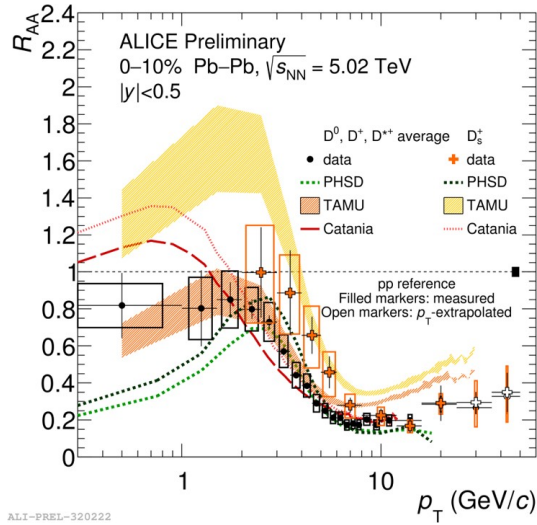
Figure 2.18: The comparison of D meson R_{AA} measured by ALICE and the heavy quark transport models [31].

2. **Thermal di-leptons** Thermal di-leptons are also produced by a QGP as same as thermal photons. Thermal photons are affected by the blue shift due to the system expansion. Hence, temperature measurements via thermal photons have large uncertainties. On the other hand, thermal di-leptons do not have the effect of blue shift because thermal di-leptons

are measured via invariant mass distribution. Therefore, they will provide precise measurements of the QGP temperature. Thermal di-leptons are the only unmeasured electromagnetic probe. Figure 2.19 shows the simulated invariant spectra of di-electrons in 0-10 % central Pb-Pb collisions at $\sqrt{s_{NN}} = 5.5$ TeV [34]. The orange line represents the contribution of thermal di-electron and the red line is the thermal radiation from the hadronic phase. The cyan line and the magenta line are decay di-electrons of hadrons and correlated $c\bar{c}$, respectively. The black line is the summation of the components. The QGP thermal radiation exceeds the hadronic thermal radiation in the mass range, $M_{ee} > 1$ GeV/c^2. Di-electrons from $c\bar{c}$ decay are the dominant background in the mass region. Therefore, measurement of $c\bar{c}$ decay di-electrons is crucial to extract the thermal di-electron component.
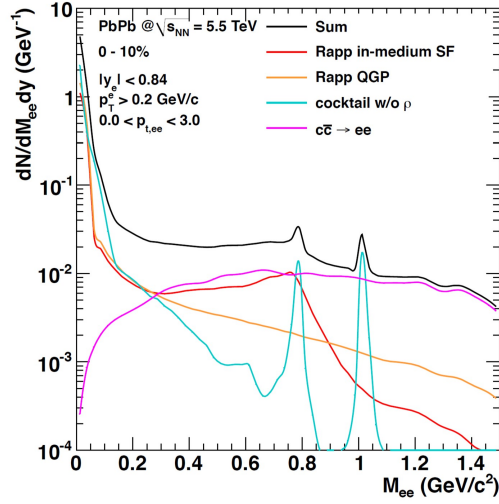
Figure 2.19: The di-electron invariant spectra in 0-10 % central Pb-Pb collisions at $\sqrt{s_{NN}} = 5.5$ TeV [34].

3. Chiral restoration The chiral symmetry breaking is the hadron mass generation mechanism. The symmetry breaking is partially restored in a high-temperature matter, however, the restoration has not been observed yet. The chiral symmetry restoration appears in modification of light vector meson masses, *e.g.* ρ. A precise measurement of low mass di-lepton spectrum is the power full way to search the chiral symmetry restoration in *AA* collisions experimentally because leptons do not interact with partons in a QGP.

Chapter 3

Trigger and data acquisition system

Many missions have been addressed at LHC as described in Chap. 2. The experiments at the LHC (ALICE, ATLAS, CMS, and LHCb) upgrade their sub-systems to achieve the missions. The increase of center-of-mass energy is limited by the difficulty of a larger accelerator construction than the LHC. Their upgrade programs are described with focusing on their trigger and data acquisition systems which are key technologies to make the breakthrough.

Largely, two strategies are proposed depending on their missions: a continuous readout system and a hardware-trigger-based system. ALICE and LHCb employ continuous readout systems. Their upgrade programs for Run 3 from 2022 are explained in the sections 3.1.1 and 3.1.2. ATLAS and CMS will upgrade their trigger systems. Their programs for Run 4 with the HL-LHC from 2027 are described in the sections 3.2.1 and 3.2.2.

3.1 Experiments with continuous readout systems

All collision event collection is ideal in large-scale hadron collider experiments. But computing performances and storage costs are not enough to allow any continuous readout systems. Consequently, we had to select events with trigger systems to reduce data volume so far. However, advances in technical tools in the last decades allow us to take all collision events. Saving raw data, which mean directly transferred and not calibrated data from detectors, is impractical even today. Therefore, an implementation of a continuous readout system with data reduction is a challenging effort.

ALICE and LHCb can employ continuous readout systems in their experimental situations and their physics requirements need continuous readout systems. While their data reduction strategies are different. ALICE needs the system to measure a wide range of transverse momentum and increase the amount of statistics for further study of the QGP properties. ALICE collects all tracks for various measurements with online calibration and tracking using detector monitoring data. LHCb requires it for *CP* violation study via heavy flavor hadron decays because LHC *pp* collisions produce too many heavy quarks to detect with its trigger system. The increase of trigger rates reached peaks of a few MHz. LHCb saves primary vertex data and tracks coming from heavy flavor hadrons. Heavy flavor hadrons decay at points distant from a primary vertex.

3.1.1 ALICE

ALICE [32] is the experiment focusing on the heavy-ion program at the LHC. The following measurements are the targets to building a greater understanding of a QGP:

- QGP density via c and b quarks dissociated measurements

- QGP temperature measurements via thermal di-leptons

- Measurements of mass modification of low mass vector mesons due to chiral symmetry restoration.

A wide range of the particle momentum region needs to be covered with particle identification for these measurements.

ALICE had collected physics data with the hardware-trigger-based data acquisition system (DAQ) [33] at a rate of 500 Hz in Runs 1 and 2. Figure 3.1 shows the architecture of the ALICE DAQ for Runs 1 and 2. The system, called the central trigger processor (CTP), selects the interaction events to meet the physics requirements. Information from triggering detectors is aggregated in the CTP. Then, the processor combines and synchronizes the trigger information. The maximum readout rate was 500 Hz in minimum bias Pb-Pb collisions.
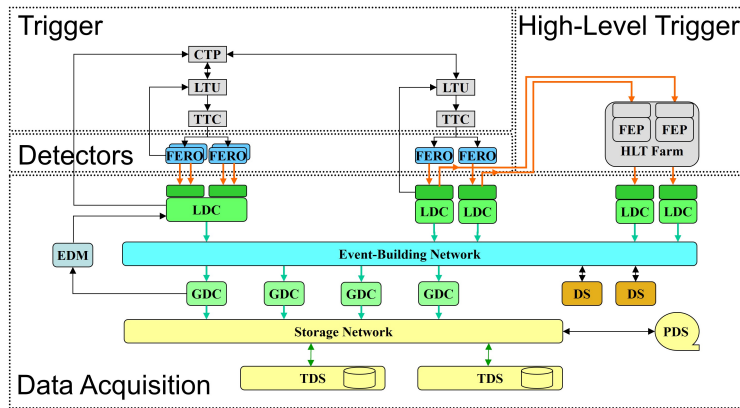
Figure 3.1: The architecture of the ALICE ALICE and trigger system [32].

The LHC increases its collision rate of Pb-Pb beams up to 50 kHz in Run 3 as described in Sec. 1.2. The time projection chamber (TPC) used in Runs 1 and 2 had limited the readout rate of 500 Hz due to a latency of the gating grid for fewer noise signals. The rate can be increased up to 3 kHz. The readout rate of the inner tracking system (ITS), which is the innermost tracking detector, is limited to up to 1 kHz. Hence, the ITS and the TPC must be upgraded to install the continuous readout system. Minimum bias data in Run 3 will be 50 times larger than the data in Runs 1 and 2 [34]. The typical volume of raw data from the sub-detectors is expected around 3.5 TB/s in the continuous readout. Storing the amount of data is hardly realized; therefore, ALICE implements the new DAQ, named the online-offline computing system (O^2) [40], to reduce the volume by online data processing.

3.1.1.1 Upgrade of central detectors

ALICE upgrades the sub-detectors to improve tracking accuracy and readout rate. Especially, replacement of the ITS and implementation of new readout boards for TPC are the

most important upgrades.

Inner Tracking System   The ITS used in Runs 1 and 2 was composed of six cylindrical layers of silicon detectors. The ITS is replaced for a new ITS which consists of seven layers of silicon pixel detectors [35]. The CMOS monolithic active pixel sensor (MAPS) technology [36, 37, 38] is employed for the silicon pixel sensors, in order to obtain high spatial resolution and reduce the material budget. The new ITS will improve the accuracy of primary vertex and secondary vertex of heavy flavor hadrons. The detection performance of low p_{T} particles will be also improved.

Time Projection Chamber   The TPC [39] is the gas detector used for charged particle tracking and particle identification (PID). The original MWPC based signal amplification system limited the trigger rate of up to 3 kHz. The TPC employs the gas electron multiplier (GEM) technology for the readout electronics to realize the high readout rate at 50 kHz in Pb-Pb collisions.

3.1.1.2   Online-offline computing system

The O^2 is a new data taking and processing system. A data throughput from the ALICE sub-detectors will reach 3.5 TB/s. It is not realistic to store the raw data in data storage. Then, the data volume is reduced with the online data process by calibration and tracking. The online tracking must keep tracking accuracy as well as the offline tracking. It is the feature of the O^2.

Figure 3.2 shows the data flow in the O^2 framework. Firstly, raw data including physics data and detector condition data are sent from the sub-detectors to FLPs which are server computers. The FLPs perform calibration and masking, which means deletion of noisy data, using the detector condition data. This process reduces the data amount from 3.5 TB/s to 500 GB/s. Then, the calibrated data are transferred from the FLPs to Event processor nodes (EPNs) where tracking is performed. The data volume is reduced from 500 GB/s to 100 GB/s. Finally, the tracking data are saved on the data storage permanently.

Here, calibration and reconstruction for the TPC data are described as an example. The TPC data throughput is evaluated around 3.4 TB/s of 3.5 TB/s [39]. Hence, reduction for the TPC data is critical in the O^2. A drift velocity and a gain depend on the temperature and pressure and the conditions are employed for online calibration and reconstruction. Additionally, front-end electronics configurations such as inactive regions are important information on the calibration and reconstruction. Firstly, zero suppression, which delete data below a threshold, and clustering using front-end configurations is performed in the calibration stage. Data which do not associated to any clusters are removed. The calibrated data are sent to EPNs and reconstructed using a drift velocity and an effective gain.

3.1.1.3   Muon Forward Tracker

ALICE installs the new silicon tracker covering the forward pseudo-rapidity region of 2.5 < $|\eta|$ < 3.6. It is the muon forward tracker (MFT) [41, 42]. The MAPS sensors used for the ITS are employed for the MFT. The MFT physics motivations are measurements of heavy quarks, thermal di-leptons, and mass modification of light vector mesons due to chiral symmetry restoration in the forward rapidity region. The rapidity dependence QGP study is crucial to understand the experimental results and to constrain models.
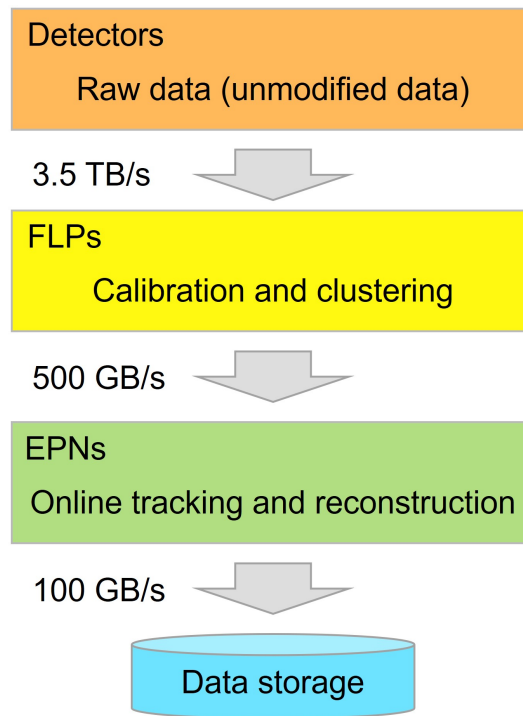
Figure 3.2: The O^2 data flow.

ALICE has measured muons in the forward region using the muon spectrometer [43, 44] . The tracking accuracy was not enough to disentangle prompt D mesons and displaced D mesons due to muon multiple scatterings inside the hadron absorber. The multiple scatterings also prevented thermal di-muon measurement and high-precision measurement of di-muon invariant mass spectrum in the low mass region. The MFT provides high-precision measurements of muons with the muon spectrometer as well as the tracking accuracy by the central detectors.

The MFT readout system follows the O^2 strategy because the MFT is the new detector. The MFT DCS also follows the upgraded ALICE DCS strategy. The design of the MFT DCS is my work.

3.1.2 LHCb

LHCb [45] is the experiment focusing on precise *CP* violation measurements via rare decays of *B* and *D* mesons described in Sec. 2.1.2 to test the standard model. A large amount of statics is necessary for these kinds of precise measurements.

LHCb had employed the trigger-based readout system in Runs 1 and 2. However, the hardware hadronic triggers, named the Level-0 trigger (L0) trigger, used in Runs 1 and 2 have limited efficiencies in higher luminosity as shown in Fig. 3.3. The vertical axis indicates the trigger yield and the horizontal axis indicates the luminosity. The black squares, the red upward triangles, the green downward triangles, and the circles represent the trigger yields of $\pi\pi$, $\phi\gamma$, $\Psi\phi$, and D_sK triggers, respectively. The yields of $\pi\pi$, $\phi\gamma$, and D_sK triggers are limited by the decision time of the triggers from the higher luminosity of around 3×10^{32} and they prevent them to take more amount of statistics. Therefore, LHCb installs the hardware trigger-less readout system, in order to collect more physics data.
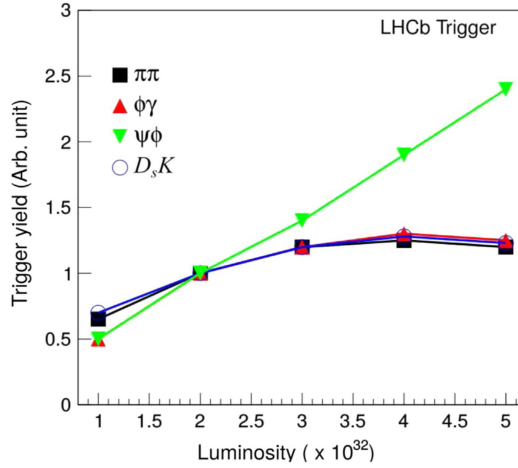
Figure 3.3: The Level-0 hardware trigger efficiency vs the instantaneous luminosity [46].

LHCb employs a continuous readout system to overcome the trigger limitations. Figure 3.4 shows schematic views of the data flow in Run 2 (left) and Run 3 (right). The trigger-based DAQ system was composed of an L0 and a software high-level trigger (HLT). The L0 reduces the event rate from the 40 MHz bunch crossing rate to the 1 MHz readout rate. The trigger rates of hadrons, single/pair muon, and electron/photon are 450 kHz, 400 kHz, and 150 kHz, respectively. Raw data of triggered events are transferred to the HLT farm. Partial reconstruction is performed using tracking information of the vertex tracker to remove events including di-muons and displaced tracks and vertices. The surviving events are buffered to disks and performed calibration and alignment on the disks.

3.1.2.1 Detectors

LHCb upgrades its detectors in order to cope with the increased luminosity and crossing rate of the LHC. Figure 3.5 describes the side view of the LHCb sub-detectors in Run 3.

Vertex detector The vertex locator (VELO) [49] is the detector surrounding the interaction point for a primary vertex decision and tracking. The distance between the detector and

Run 2 trigger diagram	Run 3 trigger diagram
40 MHz bunch crossing	**40 MHz bunch crossing**

Figure 3.4: The data flow diagrams in Run 2 (left) and Run 3 (right) from Ref. [47].

the interaction point will get close from 5 mm to 3.5 mm. The distance will enable them to improve the interaction point measurements. The VELO employs the new CMOS silicon pixel sensors to read out data at a rate of 40 MHz. The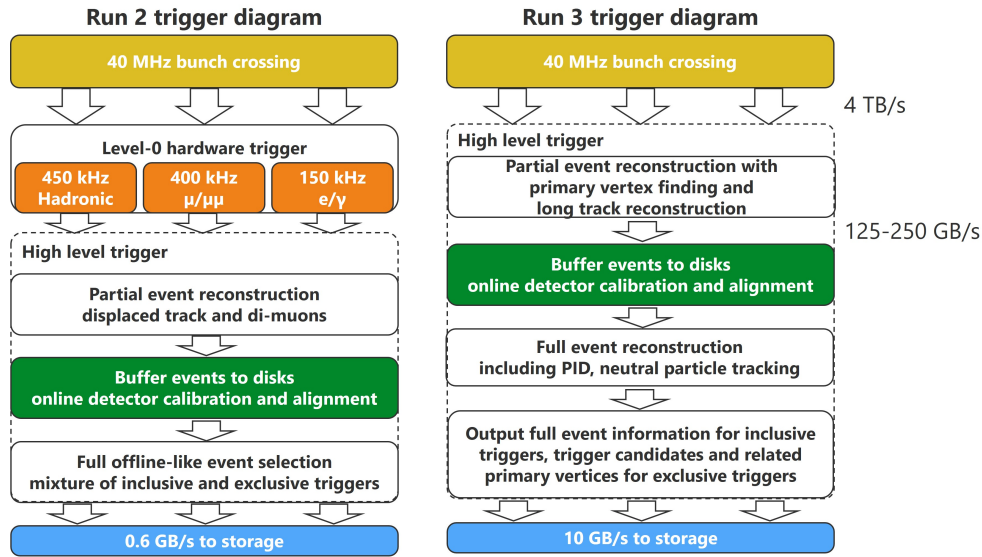 sensors will allow enhancing the tracking precision and the reconstruction speed. The size and the number of sensors will be 55μm x 55μm and 41 million, respectively.

Tracking station   The LHCb tracking system [48] will be composed of the upstream tracker (UT) and the scintillating fiber tracker. The upstream tracker will be installed between the VELO and the magnet. The tracker consists of four layers of high granularity silicon microstrip planes. The other tracker is installed on the downstream side of the magnet. The tracker will be composed of 2.5 m long fibers and the readout electronics of silicon photon-multipliers.

PID detectors   Two ring-imaging Cherenkov detectors (RICHs) [50] are installed for PID covering the full momentum range of tracks in LHCb. The RICH 1 is installed between the VELO and the dipole magnet and identifies low momentum particles of from 10 to 65 GeV/c. The aerogel radiator installed in the current RICH 1 is removed to improve material budget and PID performance. The RICH 2 is installed downstream of the tracking stations and identifies high momentum particles of from 15 to 100 GeV/c. The readout electronics will be replaced the commercial multianode photomultipliers (MaPMTs) to achieve the readout rate of 40 MHz.

3.1.2.2   Trigger and data acquisition system in Run 3

The new DAQ system is based on the Run 2 DAQ system. For the Run 3 trigger strategy, the raw data are transferred from the sub-detectors to the HLT directly. Nominal data throughput is estimated at 4 TB/s and the data are processed in the online reconstruction system.
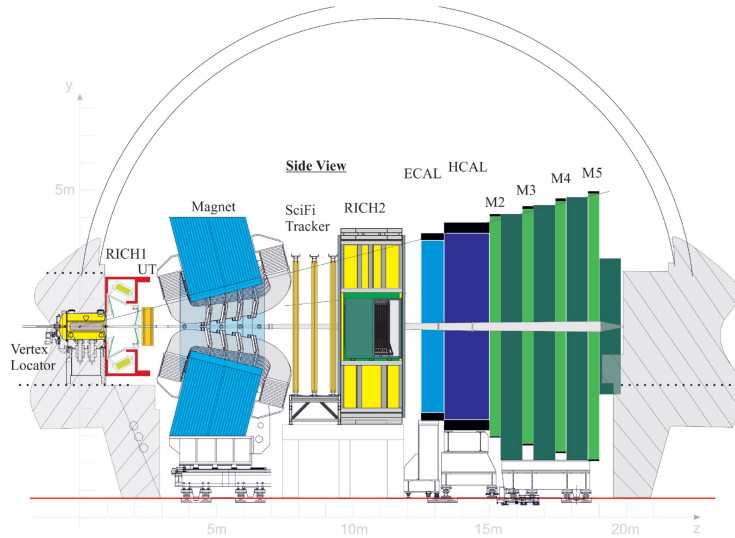
Figure 3.5: The side view of the upgraded LHCb detector [48].

Charged particles are reconstructed in the first step of the HLT. Six steps are executed on HLT1 for track and primary vertex reconstructions as sown in Fig. 3.6. Hits in the VELO are matched to form straight lines, which are called VELO tracks, loosely pointing towards the beamline. Then, the VELO track is extrapolated to the trigger tracker (TT) with a straight line to form a track, called a upstream track. At least three hits in the TT are required around the VELO track extrapolation. The TT can determine particle momentum with a relative resolution of 20 % and the momentum is used to reject low p_T tracks. Matching of long tracks with TT and the three stations (T-stations) reduces the number of fake VELO tracks. A primary vertex is also reconstructed in the HLT first step. Here, primary vertex means a proton-proton interaction point. The primary vertex, which indicates a proton-proton interaction point, is reconstructed by the VELO tracks to select displaced particles in the HLT1. The data are reduced to 125-250 GB/s at a rate of 0.5-1.5 MHz in the first step of the HLT.

The reconstructed data are archived in the buffer storage. The storage volume is 10 PB and can archive the processed data for two weeks. Then, the second step of the HLT performs offline quality reconstructions. The second step performs a full event reconstruction for the data processed. The full event reconstruction has three items: the charged particles reconstruction, the neutral particles reconstruction, and the particle identification. The reconstructed tracks decaying from heavy flavor hadrons and primary vertices are selected using decay topology of heavy flavor hadrons and save in default. In addition to this, some full event information are stored for further offline processing. The amount of data to 10 GB/s are recorded in permanent storage.
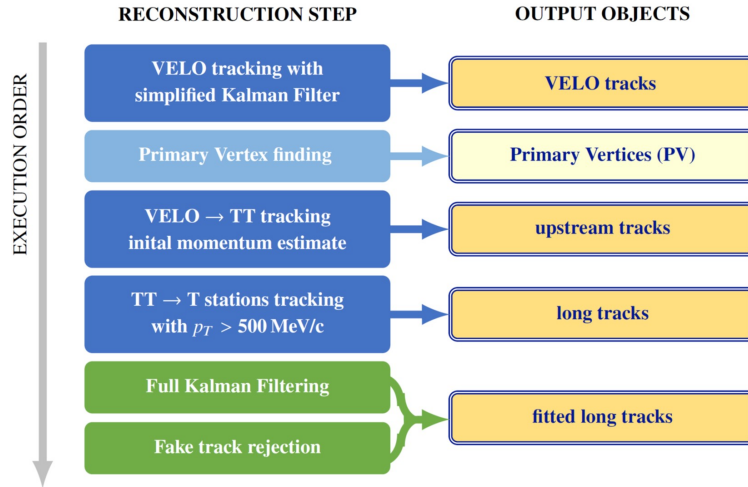
Figure 3.6: The execution order of track and vertex reconstruction on the HLT first step [51].
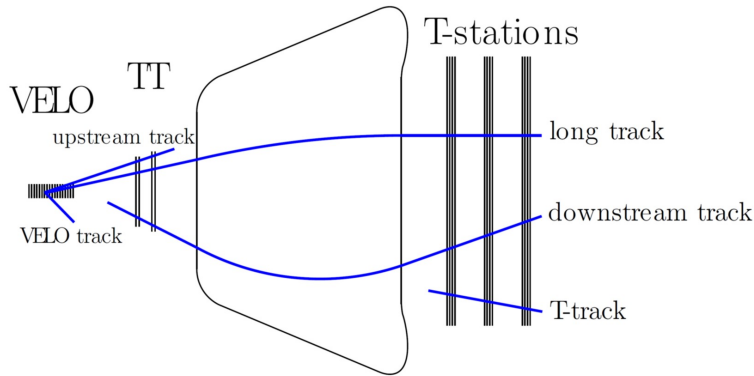
Figure 3.7: The reconstructed tracks on the HLT first step [51].

3.2 Experiments with hardware-trigger based systems

Continuous readout systems are also ideal in ATLAS and CMS. However, current computing performance and storage costs do not match their physics requirements. The estimated data volume at ATLAS and CMS are too large to process them online with current technologies. Accordingly, they will upgrade their trigger systems because their current trigger systems have room for improvement. The trigger rates will become a factor of ten faster than that of their current trigger systems. The upgraded trigger systems fully utilize the HL-LHC potential because their physics goals can be accessed only with the HL-LHC bunch crossing rate and luminosity as described in Sec. 1.2.1.

ATLAS and CMS aim at the same physics targets, the Higgs mechanism and SUSY particle search with higher precision with the HL-LHC, and have a mutually complementary relationship. The Higgs boson mass is 125 GeV/c^2 and the mass range of SUSY particles is estimated as $\mathcal{O}(100)$ GeV/c^2 – $\mathcal{O}(1)$ TeV/c^2. Their decay products should have large transverse momenta and/or large missing transverse energies. Therefore, ATLAS and CMS need various hardware triggers to select events that can produce a Higgs boson or any SUSY particles. The selected events are saved permanently on storage for offline analysis.

RECONSTRUCTION STEP	OUTPUT OBJECTS
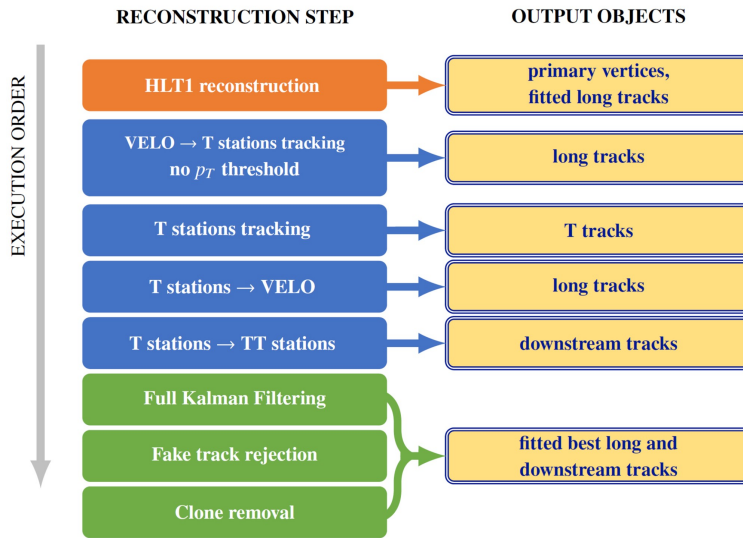
Figure 3.8: The execution order of track and vertex on the HLT second step [51].

3.2.1 ATLAS

A toroidal LHC apparatus (ATLAS) [52] is one of the general-purpose detectors for probing *pp* and *AA* collisions. ATLAS needs detectors:

- electromagnetic calorimeter for electron and photon identification,

- hadronic calorimeter for measurements of missing transverse energy and jet,

- charged particle tracker for charged leptons and heavy flavor identification,

- muon tracker for high-precision muon momentum measurement.

ATLAS has a solenoid magnet, which covers the inner detector and provides 2 T, a barrel toroidal magnet, which provides 0.5 T for the central muon detector, and endcap toroidal magnets, which provide 1 T for the endcap muon detectors. Figure 3.9 shows the schematic view of the ATLAS detector.

3.2.1.1 Detector upgrade toward Run 4

The upgrade program of ATLAS [54, 55] focuses on the Run 4 experiment with the HL-LHC. The upgraded system is called Phase-II.

Inner tracker The current Inner Detector will be replaced by a new Inner Tracker, and the Inner Tracker will be composed of the silicon Pixel Detector [56] and the silicon Strip Detector [57] for charged particle tracking. Figure 3.10 shows the layout of the ATLAS Inner Tracker. The Pixel Detector covering $|\eta| < 4$ is shown in red and the Strip Detector covering $|\eta| < 2.7$ is shown in blue.

The Pixel Detector is composed of five barrel layers and five endcap rings. The concept of the "Hybrid Pixel Detector" is a base of the Pixel Detector. 3D sensors with a pixel size of $50~\mu m^2$ and $25~\mu m^2$ for the endcap and the barrel of the innermost layer and planar sensors
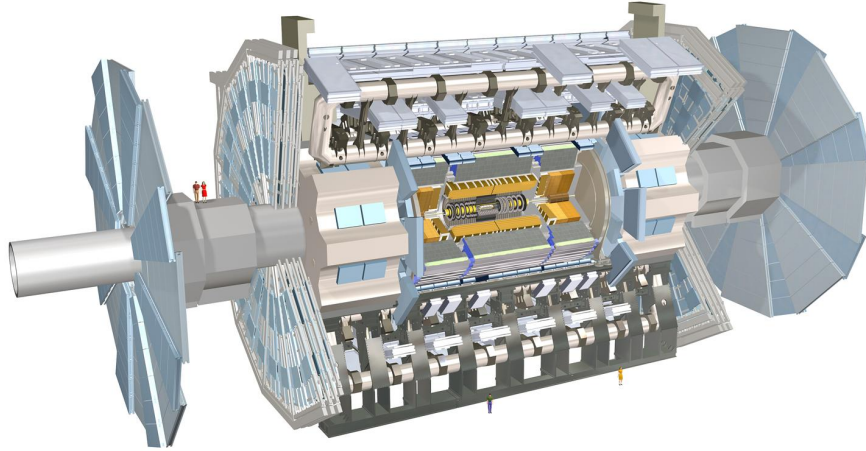
Figure 3.9: The schematic view of the ATLAS original detector [53].

with a pixel size of 50 μm^2 for the other layers are employed. The pixel sensors must have an efficiency of over 98.5 %.

The Strip Detector consists of four-barrel layers and six endcaps. Silicon micro-strip sensors are employed. The maximum readout rate of the Strip Detector for complete events is 1 MHz.
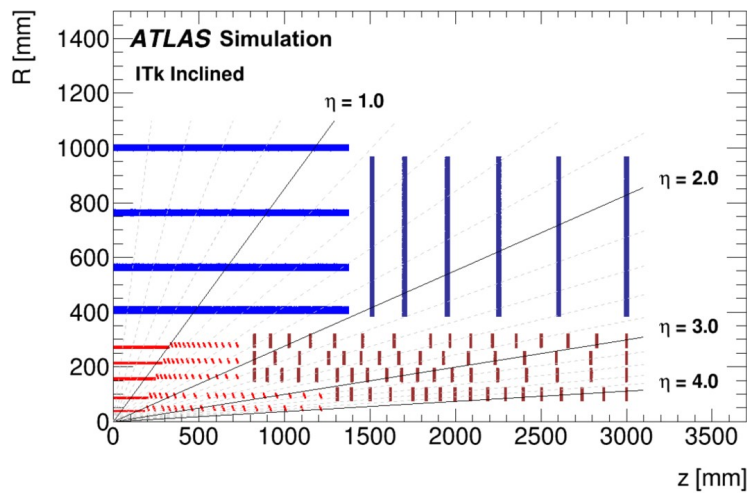
Figure 3.10: The schematic view of the ATLAS Inner Tracker [57].

Calorimeter   The liquid-argon calorimeter (LAr) [58] and the tile calorimeter [59] consist of the ATLAS calorimeter system. The upgrades for the calorimeters will be replacements of the electronics for a 40 MHz readout and will provide full granularity data.

The LAr calorimeter consists of the LAr electronic barrel, the LAr electromagnetic end-cap, the LAr hadronic endcap, and the LAr forward.

The Tile calorimeter is composed of the central parts called long barrel (LB) and the forward parts called endcap barrel (EB).
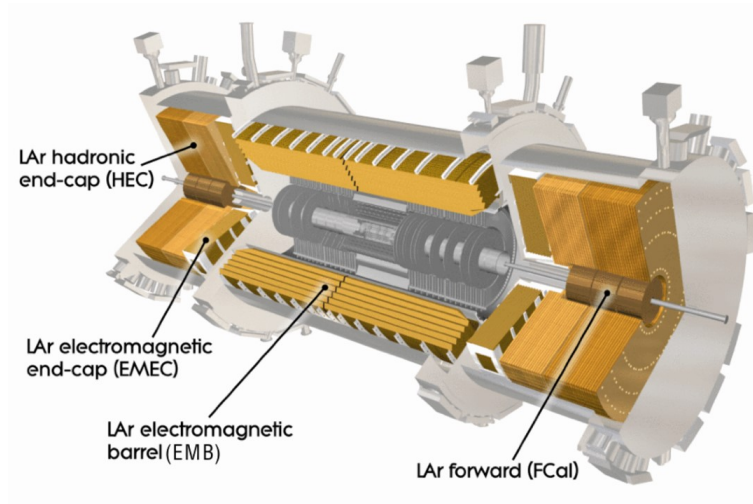
Figure 3.11: The schematic view of the LAr calorimeter [58].
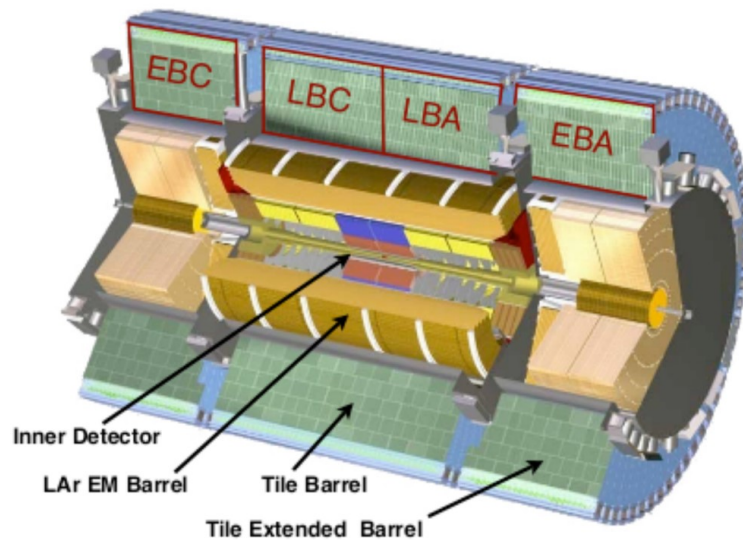
Figure 3.12: The schematic view of the Tile calorimeter [59].

Muon system   The ATLAS muon system in Phase-II [60] is composed of the three layers of resistive plate chamber (RPC) ($|\eta| < 1.05$), the three or four layers of thin gap chambers (TGC) ($1.05 \leq |\eta| < 2.4$), and the new small wheel (NSW) ($1.3 < |\eta| < 2.4$).

Hit information of the RPC and the TGC is used for muon trigger information. Also, muon tracks are measured by the RPC and TGC. The NSW consists of small-strip TGC and

micro-mesh gaseous structure chambers. The wheel is used for triggering and precision tracking.

3.2.1.2 Trigger and Data Acquisition system in Run 4

ATLAS employs the upgraded hardware trigger and DAQ, called TDAQ, toward the Phase-II experiment with the HL-LHC [61]. ATLAS will install a hardware-based Level-0 trigger (L0) to achieve the physics goals.

Table 3.1 shows the representative L0 trigger menu. H_T means a scalar sum of jet p_T in the table. The trigger system will be upgraded to achieve the 1 MHz trigger rate with the trigger menu.

Table 3.1: The representative Level-0 trigger menu in Phase-II experiment [61].

Trigger Selection	Planned HL-LHC Offline p_T Threshold [GeV]	L0 Rate [kHz]	After Regional tracking cuts [kHz]	Event Filter Rate [kHz]
isolated single e	22	200	40	1.5
isolated single μ	20	45	45	1.5
single γ	120	5	5	0.3
forward e	35	40	8	0.2
di-γ	25,25		20	0.2
di-e	10,10	60	10	0.2
di-μ	10,10	45	10	0.2
$e-\mu$	10,10	45	10	0.2
single τ	150	3	3	0.35
di-τ	40,30	200	40	0.5
single b-jet	180	25	25	0.35
single jet	400	25	25	0.25
large-R jet	300	40	40	0.5
four-jet (w/ b-tags)	65(2-tags)	100	20	0.1
four-jet	100	100	20	0.2
H_T	375	50	10	0.2
E_T^{miss}	210	60	5	0.4
VBF inclusive	2×75 w/ ($\Delta\eta > 25$ &$\Delta\phi < 2.5$)	33	5	0.5
B-physics		50	10	0.5
Supporting Trigs		100	40	2
Total		1066	338	10.4

Figure 3.13 shows the schematics of the TDAQ in Phase-II. The detectors used for triggering are the calorimeters and the muon system. The event data of the trigger detectors are transmitted to the L0 system. The L0 system decides the corresponding event data must be saved permanently or not at a rate of 1 MHz and a maximum latency of 10 μs according to the trigger menu.

A calorimeter trigger, named L0Calo, is based on the Phase-I calorimeter trigger system. Both LAr and Tile calorimeters are used as input for the calorimeter trigger. The calorimeter
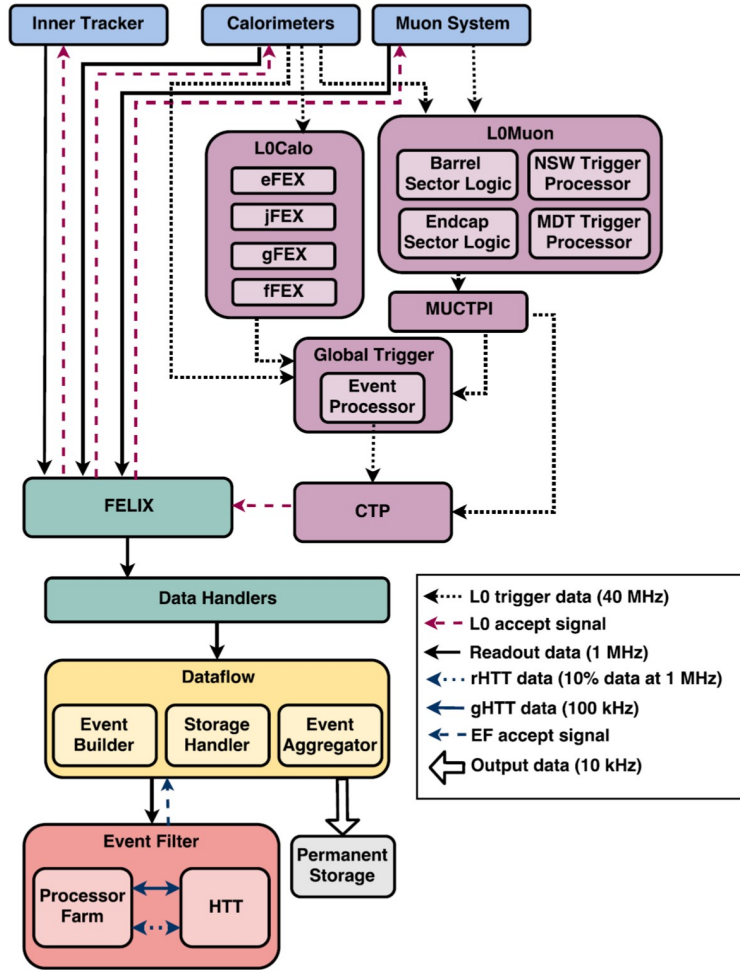
Figure 3.13: The design of the TDAQ system in Run 4 [61].

trigger system selects the events producing triggering signals of an electron, photon, tau, jet, and $E^{\mathrm{miss}}_{\mathrm{T}}$. The trigger signal is transferred to the global trigger system.

The muon trigger works for muon signals with $p_{\mathrm{T}} > 20$ GeV/c for single-lepton trigger and $p_{\mathrm{T}} > 10$ GeV/c for multi-lepton trigger at a rate smaller than 40 kHz. A momentum resolution of the muon trigger will be 5 % for 20 GeV/c muons using the muon tracks in the MDT. The muon trigger system sends a trigger signal to the global trigger and the central trigger processor.

The accepted event is aggregated at the global trigger. The global trigger complements the calorimeter trigger menu with high-granularity energy data coming directly from the calorimeters. Offline-like algorithms. In detail, the following processes are performed: topological clustering, lepton isolation, calorimeter-based pile-up suppression, jet finding, exotic object selection, and identification of electron, photon, and τ lepton are performed by the Global Trigger.

The central trigger processor (CTP) makes a final decision in the L0 trigger acceptance or rejection using the inputs from the muon trigger system and the global trigger. An accept

signal will be transferred from the CTP to the sub-detectors.

The DAQ works for data aggregate and saves into the storage when the CTP decides the trigger acceptance. The data from sub-detectors are processed by the DAQ and saved into permanent storage.

The Event Filter selects the events according to the trigger menu at a rate of 10 kHz. The Event Filter is composed of the processor farm and the hardware-based tracking for the trigger (HTT). The HTT performs an initial event selection based on the combined L0 trigger information.

3.2.2 CMS

CMS [62] is the other of the general-purpose detectors at the LHC. The detector concepts of CMS and ATLAS are different. The CMS detector design and layout aim to precise measurement of the muon momentum. CMS employs a superconducting solenoid magnet which generates a magnetic field of 4 T and a bending power of 12 Tm for high-precision measurements of muons. Figure 3.14 shows the detector schematics in Run 1.
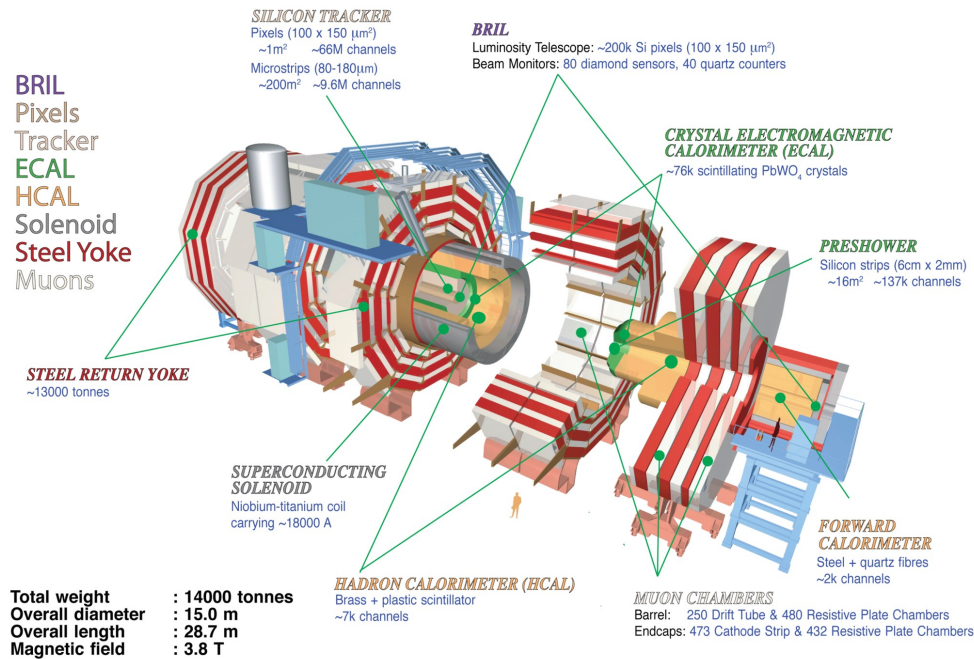
Figure 3.14: The schematic view of the CMS detector in Run 1 [63].

3.2.2.1 Upgrade toward Run 4

CMS has an upgrade program toward the Run 4 experiment with the HL-LHC. The program contains the new detector installation and the upgrade of the detectors and the online system. The upgraded detector is called the Phase-2 detector.

Tracker The CMS tracker system [64] in Run 4 is composed of an inner tracker (IT) and an outer tracker (OT) and located innermost layer of the detectors. The IT is a silicon pixel detector and the OT is a silicon strip and macro-pixel detector. The pseudo-rapidity range of the tracker is extended to $|\eta| = 3.8$.

The tracker is required to have high occupancy below the permille level in the IT and the percent level in the OT to identify the pile-up events.

Calorimeter CMS has the electromagnetic calorimeter (ECal) and the hadron calorimeter (HCal) [65, 66]. The ECal is composed of a barrel part and two endcaps. The hadron calorimeter (HCal) is composed of a barrel part, two endcaps, an outer part, and a forward part.

The barrel calorimeter indicates the barrel parts of both calorimeters and the endcap calorimeter means the endcap parts of both calorimeters. The ECal is composed of 75,848 lead tungsten scintillating crystals. For the HCal, the HCal barrel and the endcap are composed of a brass absorber and plastic scintillator. The HCal forward is a Cherenkov calorimeter.

MIP Timing Detector The ability to reconstruct the timing of most of the final state particle provides further discrimination of the interaction vertices beyond spatial tracking algorithms. A 30 ps timing resolution offsets the performance degradation due to the event pileup experienced in several observables. Global event timing can be achieved by a new timing detector sensitive to minimum ionizing particles (MIPs). The new detector installed in long shutdown 3 (2025 - mid-2027) is named the MIP timing detector [67, 68] and located between the tracker and the ECal. The MIP timing detector is composed of the barrel part and the endcap part. The MIP timing detector provides timing for individual tracks crossing it.

Muon System The muon detector [69] is the main detector in CMS. The current muon system is composed of the drift tube (DT) chambers, the cathode strip chamber (CSC), resistive plate chamber (RPC). The current muon detectors are upgraded toward Phase-II, furthermore, the new RPC detector called improved resistive plate chamber (iRPC) and the gas electron multiplier (GEM) detector will be installed in the pseudo-rapidity range of $1.8 < |\eta| < 2.4$ and $1.6 < |\eta| < 2.3$ respectively.

The muon system is also composed of the barrel region and the endcap regions. The barrel drift tube chambers cover the pseudo-rapidity range of $|\eta| < 1.2$ and the endcap cathode strip chambers cover the pseudo-rapidity range of $0.9 < |\eta| < 1.2$.

3.2.2.2 Data Acquisition System in Run 4

CMS employs Level-1 trigger (L1) trigger [71, 72] and high-level trigger (HLT) [73, 74] trigger toward Run 4. Table 3.2 shows the representative trigger menu for the CMS Phase-II experiment. H_T means a scalar sum of jet p_T in the table. CMS develops the trigger system for the trigger menu.

Figure 3.15 shows the architecture of the L1 trigger of CMS.

The trigger input detectors are the calorimeters, the muons system, and the tracking system. The estimated rates of the L1 trigger and the HLT are estimated 500 - 750 kHz.

Calorimeter Trigger The calorimeter trigger uses the combined information coming from the barrels of the ECAL and the HCAL, the endcap high-granularity calorimeter (HGCAL), and the hadron forward calorimeter (HF) to produce similar trigger performance. In Fig. 3.15, the barrels of the ECAL and the HCAL are named as the barrel calorimeter (BC). Electrons, photons, jets, hadronically decaying taus, and various energy sums are calorimeter trigger objects. The barrel calorimeter trigger (BCT) combines the information of the ECAL and the HCAL. The trigger information of the BCT and HF are transferred to the global calorimeter trigger (GCT). The GCT sends the HF and the BCT information to the correlator trigger (CT). And then it combines the BC, the HF, and HGCAL information to calculate the trigger objects and send them to the global trigger. Data transfer from the GCT to the CT is performed

Table 3.2: The representative Level-1 trigger menu in the Phase-II experiment based on Ref. [72].

L1 Trigger seeds	Offline Threshold(s) at 90% or 95%(50%) [GeV]	Rate $< PU >= 200$ [kHz]	Additional Requirement(s) [cm, GeV]	Objects plateau efficiency [%]
Single TkMuon	22	12	$|\eta| < 2.4$	95
Double TkMuon	15,7	1	$|\eta| < 2.4, \Delta z < 1$	95
Single TkElectron	36	24	$|\eta| < 2.4$	93
Single TkIsoElectron	28	28	$|\eta| < 2.4, \Delta z < 1$	93
Double TkElectron	25,12	4	$|\eta| < 2.4$	93
Single TkIsoPhoton	36	42	$|\eta| < 2.4$	97
Double TkIsoPhoton	22,12	50	$|\eta| < 2.4$	97
Single CaloTau	150(119)	21	$|\eta| < 2.1$	99
Double CaloTau	90,90(69,69)	25	$|\eta| < 2.1, \Delta R > 0.5$	99
Single Jet	180	70	$|\eta| < 2.4$	100
Double Jet	112,112	71	$|\eta| < 2.4, |\eta| < 1.6$	100
H_T	450(377)	11	jets: $|\eta| < 2.4, p_\mathrm{T} > 30$	100
$E_\mathrm{T}^\mathrm{miss}$	200(128)	18		100

within 5 μs and transfer from the GCT to the global trigger is performed within 9 μs to keep the bunch crossing rate.

Muon Trigger   The muon trigger is employed to identify muon tracks. The trigger uses the information of standalone muon tracks reconstructed in the muon detector and matching muons from the L1 track finder. The trigger uses all muon detectors of the drift tube (DT), the resistive plate chamber (RPC) including the improved resistive plate chamber (iRPC), cathode strip chamber (CSC), and the gas electron multiplier (GEM) detector.

The muon trigger system has three track finders each pseudo-rapidity regions: the barrel muon track finder (BMTF) ($|\eta| < 0.8$), the overlap muon track finder (OMTF) ($0.8 < |\eta| < 1.2$), and the endcap muon track finder (EMTF) ($1.2 < |\eta| < 2.4$) because the detector technologies and conditions are different. Then, the outputs of the track finders are transmitted to the global muon trigger which reconstructs global muons and tracker muons. The global muon trigger also receives signals from the barrel layer-1.

Global Track Trigger   The global track trigger is a newly installed trigger system in the L1. It builds high-level objects out of the tracks within the full outer silicon tracker volume. The inputs of the global track finder come from the track finders. The Global Track Trigger plays a role to build high-level objects out of the tracks.

Correlator Trigger   The object of the correlator trigger system is to aggregate inputs from all upstream systems and optimally combine the information from the various sub-systems to achieve the best possible trigger performance for the most challenging physics topologies. The correlator trigger is composed of two particle-flow layers as shown in Fig. 3.15. The
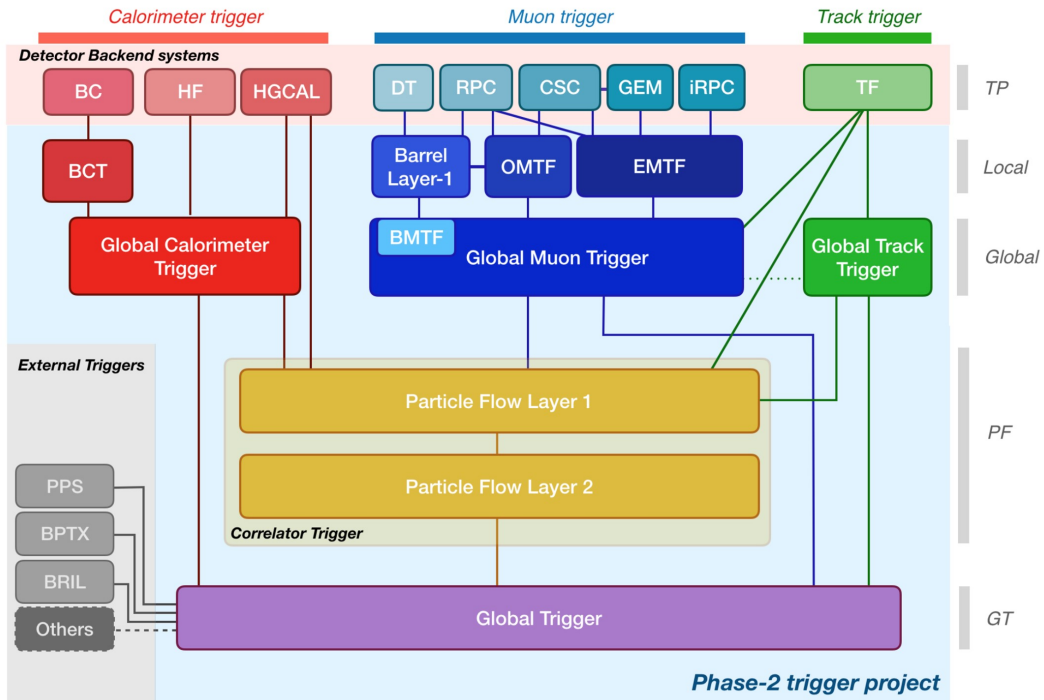
Figure 3.15: The architecture of the CMS trigger [72].

first layer creates particle-flow candidates, which the PUPPI [75] algorithm defines, and the created candidates are transferred to the second layer. The second layer reconstructs physics objects, such as electrons, jets, and $E_{\mathrm{T}}^{\mathrm{miss}}$.

Global Trigger The trigger menu is implemented on the global trigger. The global trigger processes the inputs from the upstream trigger systems and decides the trigger type based on the trigger algorithms. The outputs of the global trigger are transmitted to the Phase-II Timing and Control Distribution.

Chapter 4

Summary and discussion

The modern particle physics has progressed with the advancements of technologies, especially accelerators. However, it is very hard to make a significant increase of center-of-mass energy by making an accelerator larger. The only achievable accelerator improvement is an increase of a luminosity for the next decade.

New trigger and data acquisition systems are mandatory to follow the increase of the luminosity at the LHC. ALICE and LHCb employ continuous readout systems. A continuous readout system takes all collision events without any hardware triggers. Technological advances in the last decade enable us to realize continuous readout systems. Although, raw data recording is unattainable with the current technologies. For that reason, data reduction by calibration and reconstruction is a key factor in a continuous readout system. ALICE requires all information in Pb-Pb collisions at 50 kHz for the QGP property study. The amount of raw data from sub-detectors is estimated as 3.5 TB/s. ALICE reduces the data amount from 3.5 TB/s to 100 GB/s by online calibration and reconstruction using detector conditions. While, the hardware trigger rate of LHCb used in Runs 1 and 2 was 1 MHz by the decision time of the hardware trigger and great improvements of the trigger system could not be expected technically. Therefore, LHCb need the continuous readout system to collect all collision events in pp collisions at a rate of 40 MHz CP violation measurements via rare decays of heavy flavor hadrons. In the situation, the data volume is estimated as 4 TB/s. LHCb reduces the data volume by online calibration, reconstruction, and selection. The system records primary vertices and tracks of heavy flavor decay products using decay topology of heavy flavor hadrons. Thereby, the amount of data are reduced from 4 TB/s to 10 GB/s by the processes. On the other hand, ATLAS and CMS improve their hardware trigger systems. Their upgrades concentrate on the study of the Higgs mechanism and new particle searches with the HL-LHC. The data volumes of ATLAS and LHCb with the HL-LHC are estimated as 200 TB/s and 336 TB/s, respectively if they employ continuous readouts. Their data amounts are too large for to employ continuous readout systems with moderate efforts. Additionally, their trigger system have room for improvement and the rates of the upgraded trigger systems will be larger by a factor of ten than that of their current systems with maximum efforts. Therefore, the trigger system upgrades are the reasonable solutions. However, their trigger rates are getting close to the limit. All collision event recording is ideal in any hadron collider experiments even ATLAS and CMS like experiments. Further technological innovations in future will allow us to employ continuous readout systems in any collider experiments and ATLAS and CMS will move from the trigger systems to continuous readout systems. The features of the new trigger and DAQ are summarized as shown

on Tab. 4.1.

Table 4.1: Comparison between the strategies of the each experiments.

	Hardware trigger	Software trigger	Online tracking	Other features
ALICE	✗	✗	✔	All information recording
ATLAS	✔	✔	✗	1 MHz trigger
CMS	✔	✔	✗	750 kHz trigger
LHCb	✗	✔	✔	Online event selection

We should aim for continuous readout systems and ALICE is one of the frontiers in this field. The O^2 requires the new control and monitoring scheme to realize the online calibration and reconstruction using detector condition data. The new control and monitoring scheme is demonstrated in the control system for the muon forward tracker (MFT) newly installed in the forward rapidity region. It is a model case for the O^2 and the new scheme.
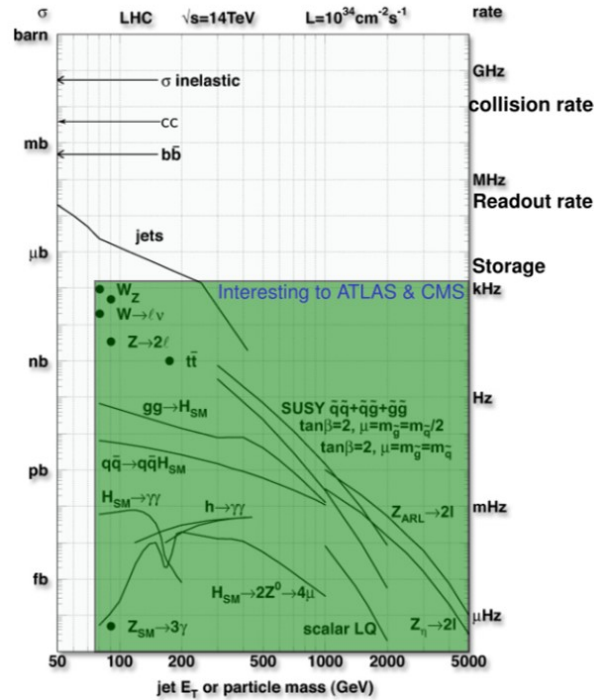

Figure 4.1: The cross-section and the generation rate vs the jet E_T or particle mass with the LHC luminosity and energy [76].

Part II

Detector control system for the muon forward tracker

Chapter 1

Detector control system at ALICE

Dada reductions by online calibration and reconstruction with data conditions are crucial in the ALICE O^2 project. Raw data which are composed of physics data and detector conditions are transferred in the same data segments from the sub-detectors to the processors for effective calibration. Raw data of 3.5 TB/s are reduced by a factor of seven in the calibration step. Previously, the DAQ and the control system were completely different systems and physics data and detector conditions were transferred separately because calibration and reconstruction were performed offline. However, the DAQ and the control system become one flesh in the O^2. Therefore, a new detector control and monitoring scheme is required to achieve the physics goals with the O^2.

1.1 Basics of a detector control system

The detector control system (DCS) is responsible for detector operation, monitoring, safety, and reliable experiment. A new control and monitoring scheme is necessary to implement the continuous readout system with data reduction. The basic concept of a DCS and the new DCS scheme are described in this section.

A DCS is based on a distributed control system. Distributed control systems are commonly used in detector control systems and accelerator control systems because the distributed system has some advantages. For instance, simplified hard-wiring, scalability, and flexibility. In the distributed system, computers assigned to constituent devices, are connected via Ethernet as shown in Fig. 1.1. We can add and exclude devices easily connecting and disconnecting Ethernet cables. In case of some failures, the distributed system allows experts to separate the failure devices from the entire system.

A DCS is composed of three layers: a supervision layer, a process management layer, and a filed management layer. Figure 1.2 shows the DCS layers. The supervision layer is composed of software components, *e.g.* supervisory control and data acquisition (SCADA), algorithms for control, and a graphical user interface (GUI). A SCADA provides tools for a GUI which shows operation panels and parameters on displays. Some algorithms run on a SCADA system. Operators work their tasks using a SCADA. The process management layer is comprised of computers and hardware elements. programmable logic controller (PLC) and power supply systems are in the process management layer. Detector front-end electronics and sensors are the elements of the field management layer.

SCADAs play an important role in the DCS. The SCADA visualizes control commands of the system detector status collected via the network. Operators and detector experts han-
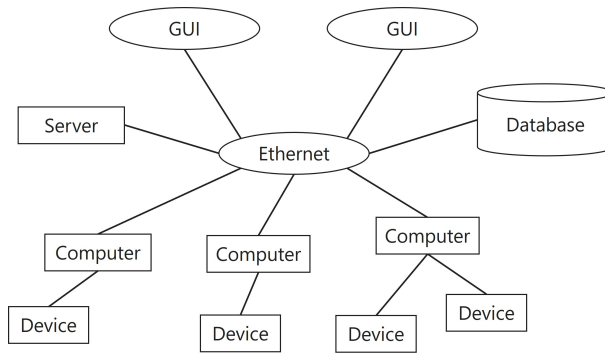
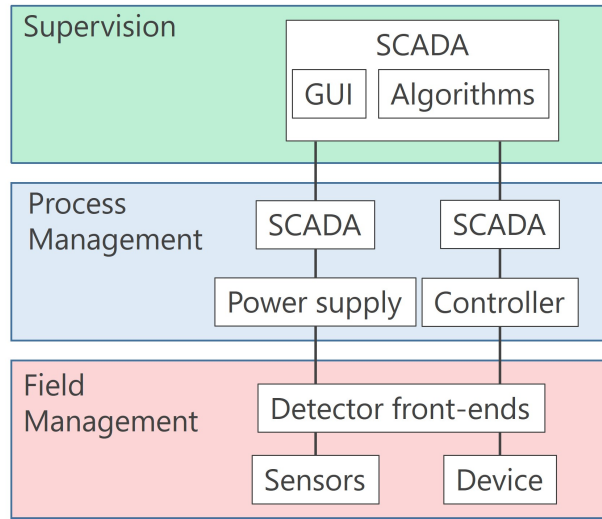Figure 1.1: The schematic view of the distributed control system.

Figure 1.2: The image of the DCS layers.

dle the detectors with the SCADA installed in the supervision layer. Ethernet connects the SCADA in the supervision layer and the SCADAs in the process management layer as the distributed system. The SCADA commonly used at CERN is WinCC open architecture (WinCC OA) [77] produced by SIEMENS.

A finite state machine (FSM), also called an automaton, is an abstract machine. The FSM definitions are as follows:

- It must have some states;

- It transits the states in response to inputs;

- It may output upon its state and input.

The FSM is designed based on detector behaviors in the DCS. The sub-detectors are operated by commands corresponding to a state implemented on the FSM. The commands can prevent unexpected operations by operators.

A safety system is also managed by the DCS. The safety system consists of a software interlock and a hardware interlock. The software interlock is triggered with minor issues such as power supply system channel trip. The software interlock is based on an FSM. When

an element state is an error, the software interlock turns off relevant elements. The hardware interlock is caused by major issues, for instance, significant overheat of the detector and cooling system failure The hardware interlock is based on PLCs, on which alarm handling and automated actions are programmed detector by detector. When a major issue happens, the hardware interlock stops all ALICE sub-detectors and data taking.

1.1.1 New control and monitoring scheme

The ALICE DCS also plays an important role in the O^2 strategy, because online calibration and reconstruction require the DCS data such as detector temperatures and voltages. The ALICE DCS needs to introduce a new control and monitoring scheme to achieve the physics goals with the O^2.

In the system used in Runs 1 and 2, physics data and detector conditions were transferred separately in different lines because calibration and reconstruction were performed offline for physics data saved on the permanent storage using detector conditions. However, the O^2 executes calibration and reconstruction online to reduce the amount of continuously read physics data before physics data are saved on permanent storage. Especially, calibration is carried out on the FLPs right after data taking. Detector conditions need to be delivered with physics data simultaneously for online calibration. The ALICE low-level front-end (ALF), the front-end device (FRED), and the ALICE datapoint service (ADAPOS) are developed as the new ALICE DCS scheme to follow the O^2 strategy [78, 79].

Figure 1.3 shows the schematic view of the ALICE DCS data flow. The raw data, including physics data and the DCS data, are transferred in the same data paths, for which giga-bit transceiver (GBT) developed by CERN is employed, from the detectors to the FLPs. Calibration is performed on the FLPs and then the raw data are divided into the physics data and the DCS data on the FLPs. Then, the physics data are transferred to the EPNs and the DCS data are transferred to the SCADA via the FRED. The DCS data are stored on the DCS database. The ADAPOS publishes the corresponding DCS data from the DCS database to the EPNs and the EPNs perform reconstruction using received DCS data.
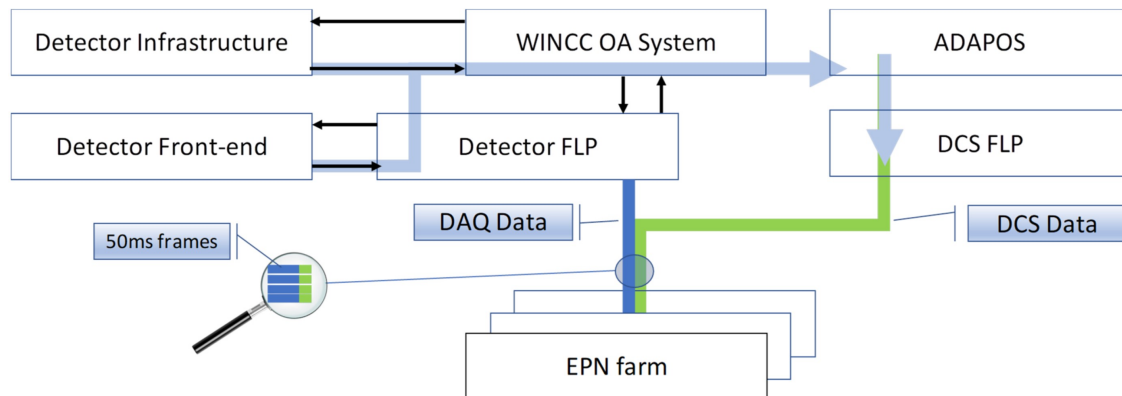

Figure 1.3: The DCS data flow in the new ALICE DCS framework [78].

ALF-FRED architecture The FRED is a computing server installed between the FLPs and the SCADA communicating with Ethernet. Operation commands written in a high-level

language are translated into command sequences written in a low-level language for the GBT slow control adaptor (GBT-SCA).

Also, monitoring data written in hexadecimal sentences are converted into numerical values. The ALF is software for data exchange between the FLP and the FRED and installed on the FLP.

ADAPOS   ALICE datapoint service (ADAPOS) is a new data transfer system in the DCS data facility. The EPNs need the detector condition parameters collected by the DCS to perform track reconstruction. The ADAPOS publishes the conditions from the DCS database to the EPNs, when the detector conditions are updated.

The new DCS for the sub-detectors must be designed and developed based on the new control and monitoring scheme to realize the continuous readout system with online calibration and reconstruction and achieve the physics impact.

1.2   Scope of this part

The ALICE DCS upgrades its scheme as a part of the O^2 to achieve the ALICE physics goals because he new ALICE DCS is a crucial scheme to realize online calibration and reconstruction using detector conditions. The MFT is the new detector and the DCS for the MFT is firstly developed based on the new ALICE DCS scheme.

Chapter 2

Muon forward tracker

ALICE measured muon tracks with the muon spectrometer in the forward region. The results in Run 1 showed that more precise measurements in low-p_T down to 0.5 GeV/c and disentanglement of heavy flavor hadrons are needed for further study of the QGP properties. The MFT is the new silicon pixel detector to improve the tracking accuracy of muons.

2.1   Muon measurements at ALICE

Muon measurements were performed with the ALICE muon spectrometer in the forward rapidity region ($2.5 < |\eta| < 4$) and many brilliant results were reported. However, the results from Run 1 data also showed that we need more precise measurements of low-p_T heavy quarkonia, heavy flavor hadrons, and low invariant mass di-muons for the understanding of the QGP properties.

The hadron absorber is set between an interaction point and the muon spectrometer to reduce background signals, such as electrons and hadrons. The absorber has a length of 4.13 m and is composed of carbon and concrete (~10 λ_{int}, ~60 X_0). Muon multiple scatterings in the hadron absorber prevented high accuracy muon tracking.

To improve the accuracy, the new silicon detector, named the MFT, is installed between an interaction point and the hadron absorber. The MFT covers the forward pseudo-rapidity range of $2.5 < |\eta| < 3.6$ The MFT tracks muons before traversing the absorber and matching of muon tracks reconstructed by the MFT and the muon spectrometer respectively will improve the accuracy of primary vertex reconstruction.

2.2   Detector setup

The MAPS technology [36] silicon pixel sensors, named ALPIDE [37, 38], are employed for the MFT because the MAPS technology have a lot of advantages, in terms of power consumption, readout speed, and radiation tolerance. In addition, noise-less signals are collected because the readout and analog-to-digital conversion are performed in parallel. The ALPIDEs realize a spatial resolution of 5 μm. The size of an ALPIDE chip is 1.5×3 cm^2 and the pixel pitch is 27×27 μm^2. 936 chips are implemented on the MFT.

Figure 2.1 shows the three-dimensional image of the MFT. The MFT consists of two half cones, called the top and the bottom. The half cones have the same structure. Five half discs, which is composed of two detection planes, constitute the half cone. The discs are
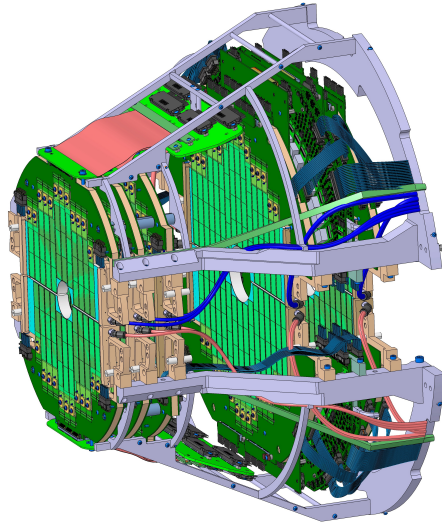
Figure 2.1: The three-dimensional image of the MFT [82].

numbered zero to four from the side close to the interaction point. One detection plane is placed on the vertex point side and the other is placed on the absorber side. A detection plane contains 12 to 17 ladders, which are flexible printed circuit boards with two to five ALPIDE chips. A set of two to five ladders consists of a zone, which is a minimum unit for readout, to save connection lines as shown in Fig. 2.2. The line from the readout unit (RU) links up to a single zone. A power supply unit (PSU) and PSU mezzanine cards are placed between half-disc 3 and disc 4. The PSU houses DC-DC converters to provide stable power and to prevent voltage drops. There are the GBT-SCA on the mezzanine cards for the DCS data exchange.

zone 0 | zone 1 | zone 2 | zone 3
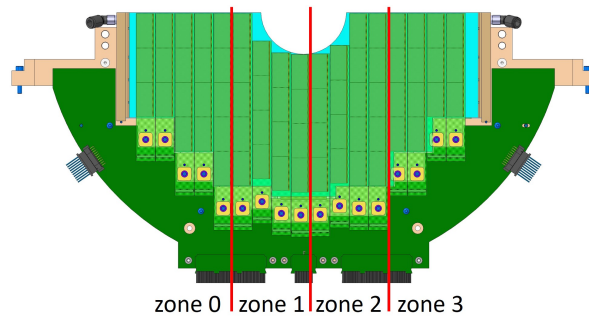
Figure 2.2: The example of the zones of the half detection plane [82].

The MFT frontend electronics (FEE) cards are based on a field programmable gate array (FPGA) system, calling RU. The RUs enable to read raw data including physics data and DCS data. One RU is assigned to one zone and reads the raw data from the zone. The RU configures the ALPIDE chips on the corresponding zone. A GBT-SCA is used for the RU control and configuration.

Chapter 3

Design of the detector control system

The architecture of MFT DCS is based on the new ALICE control and monitoring scheme to employ the O^2. The control system is composed of a power supply system, a cooling system, and a control & readout system. Modules produced by CAEN are employed as the power supply system for the MFT. For the cooling system, a water cooling system is employed. In addition to this, a ventilation system is used as the detector cooling system. The water cooling and ventilation systems are managed by the CERN cooling and ventilation group. The MFT is operated and monitored via the FSM which has a tree structure based on the detector structure including the RUs, the power supply system, and the cooling system. The FSM also contains a software interlock system which handles minor issues such as excess of a temperature. Moreover, the hard-wired safety system, named a detector safety system, is employed to handle major issues *e.g.* a failure of the cooling system.

3.1   Overview

The DCS for MFT is designed based on the upgraded ALICE DCS strategy and framework. WinCC open architecture (WinCC OA) and a joint control project (JCOP) framework [80], are applied for the MFT DCS software because they are provided by CERN and officially supported tools. The MFT DCS has a distributed structure composed of three systems: a power supply system, a cooling system, and a control & readout system as shown in Fig. 3.1. Two steps interlock systems, namely the software interlock and the hardware interlock, are implemented as the safety system.

3.2   Power supply system

The power supply system provides low-voltage power of a few volts to the MFT and the RUs. The ALPIDE needs two lines of 1.8 V for analog and digital parts and a bias voltage of -3 V for the silicon sensor via the PSUs, which house several DC-DC converters, in order to prevent voltage drop. The distance between the detector and the power supply system is around 40 m. The PSU also provides 1.8 V power to the GBT-SCA and readout unit (RU).

The system manufactured by CAEN [81] is employed for the MFT power supply system as shown in Fig. 3.2. An SY4527 is a mainframe to house two branch controllers, numbered A1676A, and allows the entire power supply system from WinCC OA via Ethernet. The controllers are needed for the embedded assembly system (EASY), which is the magnetic
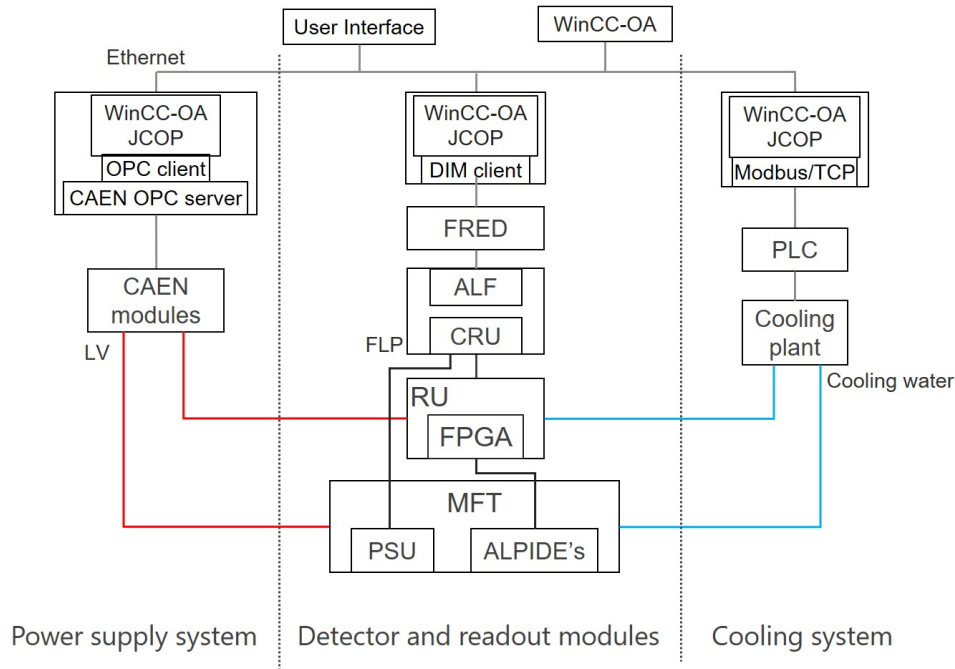
Figure 3.1: The schematic view of the MFT devices [82].

field and radiation tolerant power supply system. Two EASY systems are implemented in the MFT DCS. One supplies power to the PSUs and the other supplies power to the RUs. Four EASY3000 crates powered by four A3486 house twelve A3009 boards and two A3006 boards. A3486 is a 3-phase 400 V_{ac} to 48 V_{dc} converter designed for the EASY implementation.
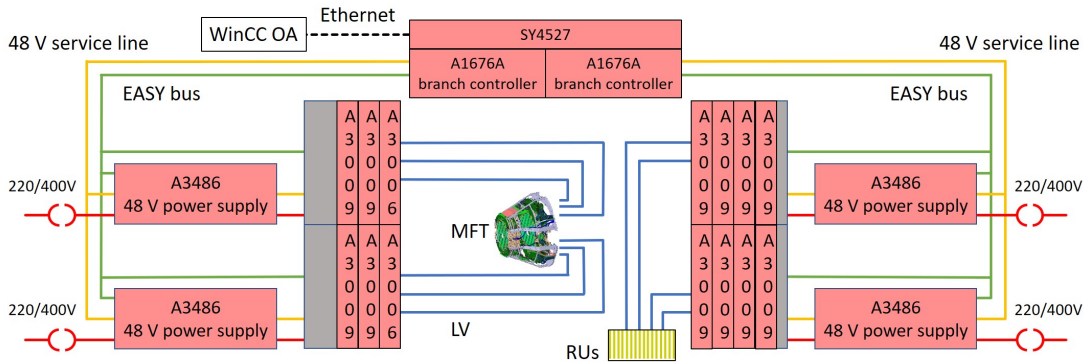
Figure 3.2: The architecture of the MFT power supply system [82].

3.3   Cooling system

A leak-less water cooling and an air ventilation system are employed for the MFT detector. The RUs are cooled by the water cooling system. Figure 3.3 shows the setup of the water cooling system for the MFT. The pressure value of the water cooling system is 0.3 bar since the pressure is lower than the atmospheric pressure so as to avoid water leaks. The nominal

temperature ranges of inlet water to the MFT and the RUs are 18–20 degrees Celsius and 18–23 degrees Celsius, respectively.

The air cooling system guarantees the temperature and humidity inside the detector volume with the flow of dry and cool air. The air temperature is 20 degrees Celsius and the humidity is 35 %. The parameters of both cooling systems are monitored by the DCS and used for inputs of the interlock system. The CERN ventilation group manages the cooling systems.
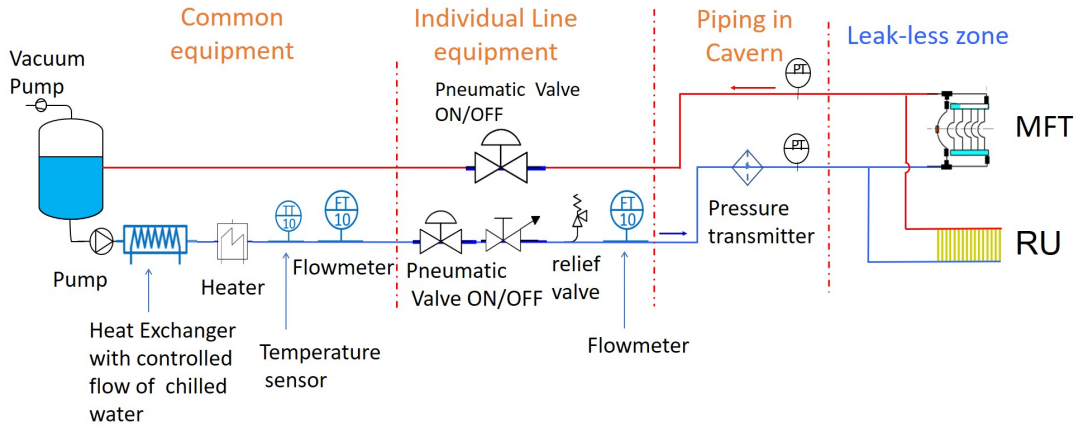

Figure 3.3: The water cooling system for the MFT detector and the readout units [82].

3.4   Control and readout system

The MFT components are operated and monitored via the ALF-FRED and FLP. One FRED and 40 FLPs with two CRUs each are implemented in the system for raw data process and DCS data transfer. The components are 80 RUs, four mezzanine boards, four PSUs, and 936 ALPIDEs in total. The RUs and the mezzanine boards house the GBT-SCA chips for configuration and monitoring of the RUs and of the ALPIDEs Temperature sensors are mounted on the ALPIDEs, GBT-SCAs, the mezzanines, the half-planes, the RUs, and the FPGAs on the RUs.

3.5   Control scheme

The MFT is operated via the FSM. The FSM has a tree structure based on the MFT hardware structure as shown in Fig. 3.4. A control unit is a conceptual classification to control and monitor smaller structures of the detector effectively. A detector unit is an actual device and must have some states even if states can be OK and ERROR only. We can control and monitor the whole detector equipment from the top node, named MFT. Commands are transferred from the upper nodes to the lower nodes. States of the device units are referred by the control units just above the device units.
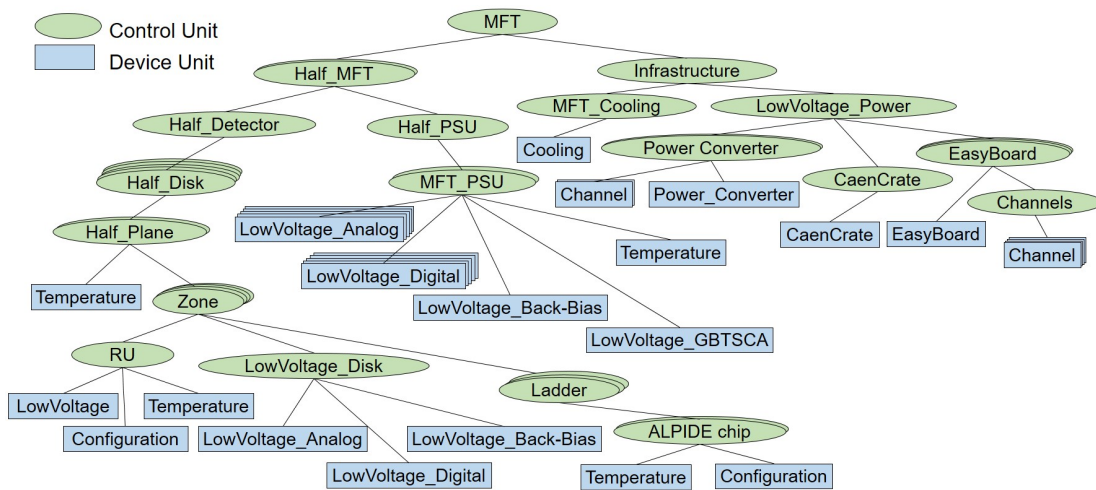
Figure 3.4: The tree structure of the MFT control system [82].

3.6 Safety system

A software interlock system and a hardware interlock system are employed as the safety system for MFT. Minor issues are handled by the software interlock and problems, which the software interlock cannot take care of.

The software interlock is implemented on the FSM. FSM outputs stop the relevant power supply channels when a detector element parameter overs a threshold. Temperatures of the GBT-SCAs, the half-planes, the RUs, the FPGAs on the RUs, the mezzanine boards, and the ALPIDEs are monitored. FSM turns all channels of the power supply system if one of the flows or the humidity of the ventilation air or temperature of a half-disc shows an abnormal value. In addition to interlock triggering the temperature and the air aberrations, the software interlock system triggers communication loss between WinCC OA and the FRED and/or the FLP and between WinCC OA and the power supply modules.

The hardware interlock design for MFT triggers communication loss between WinCC OA and the CAEN mainframes and excessive over the temperature of the detector. Any troubles with the water cooling system are handled by the hardware interlock.
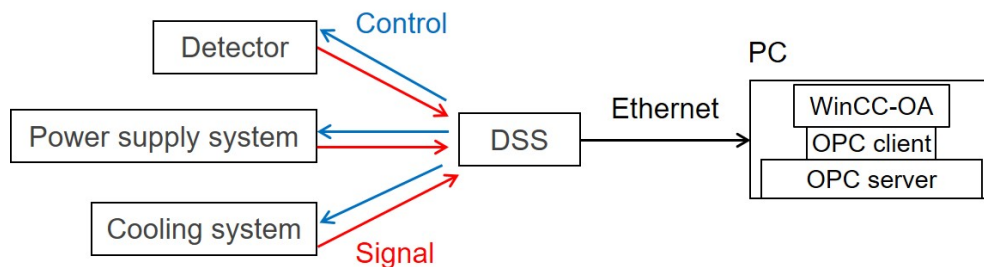

Figure 3.5: The DCS data flow for the MFT [82].

Chapter 4

Conclusion

Recording of all collision events is ideal in collider experiments. Recent technological improvements allow us to take all collision events, nonetheless, saving of data without any modification is unrealistic. For that reason, data reduction by calibration and reconstruction is crucial in case of a continuous readout system employment.

ALICE and LHCb employ continuous readout systems. The online computing system of ALICE reduces the data amount by online calibration and reconstruction using detector condition data. It records tracks as much as possible in Pb-Pb collision events. The LHCb system selects tracks by the decay topology of heavy flavor hadrons in a whole pp collisions. On the other hand, ATLAS and CMS, whose programs concentrate on data taking with the higher luminosity, improve their hardware trigger systems, expressly the trigger rates, because it is more challenging for them to have continuous readout systems. Additionally, the faster hardware triggers match their physics requirements with reasonable efforts to record their interested events. The extremely larger data volumes taken by ATLAS and CMS than that of ALICE and LHCb prevent them to take a whole of pp collisions. However, the trigger rates of their upgraded trigger systems approach the technical limitation continuous readout systems can be the best choice for any experiments. Further technology innovations will allow to record all collision data with continuous readout systems even with much higher luminosity.

A continuous readout system is the future direction for hadron collider experiments. ALICE leads the field of continuous readout systems. ALICE reduces the data volume by calibration and reconstruction with detector conditions. The control and monitoring system for sub-detectors and the physics data processing system were separated. However, raw data including physics data and detector conditions need to be transferred in the same data stream from sub-detectors to processors for effective data reduction. Physics data calibration is performed using the detector conditions *e.g.* temperatures and voltages and front-end electronics configurations such as inactive regions on the processors. Accordingly, the calibration and the reconstruction reduce the data volume by a factor of seven a factor of five, respectively. The new detector control and monitoring scheme is required to realize the online data reduction.

The new detector control system is implemented and demonstrated for the MFT, which is newly installed in the forward pseudo-rapidity region, from scratch. The control system is composed of the power supply system, the cooling system, and the communication system which is the new scheme. It is the first control system following the new control and monitoring scheme. The new control scheme is a model case for a continuous readout system and

online data reductions.

The control system is made a final adjustment toward the next Run and a pilot run is performed in 2021. A pilot run is a performance test with proton beams without accelerating at a 600 Hz trigger rate. It is conformed that the MFT and the new readout system including the new control and monitoring scheme work correctly. The ALICE Run 3 experiment will start in this year. The new ALICE will progress particle physics.

Acknowledgment

Bibliography

[1] P. K. Sigg, *Rf for cyclotrons*, CAS - CERN Accelerator l : small accelerators, pp.231-251, DOI 10.5170/CERN-2006-012.231

[2] F. Halzen and A. D. Martin, *Quarks and Leptons*, John Wiley & Sons, Inc..

[3] S. Myers and H. Schopper (editors), *Particle Physics Reference Library Volume 3 Accelerators and Colliders*, Springer Open, $DOI : 10.100/978 - 3 - 030 - 34245 - 6_7$.

[4] V. E. Barnes *et al.*, *Observation of a Hyperon with Strangeness Minus Three*, Phys. Rev. Lett. 12, 204 (1964).

[5] J. J. Aubert *et al.*, *Experimental Observation of a Heavy Particle J*, Phys. Rev. Lett. 33, 1404 (1974).

[6] J. E. Augustin *et al.*, *Discovery of a Narrow Resonance in e^+e^- Annihilation*, Phys. Rev. Lett. 33, 1406 (1974).

[7] S. W. Herb *et al.*, *Observation of a Dimuon Resonance at 9.5-GeV in 400-GeV Proton-Nucleus Collisions*, Phys. Rev. Lett. 39, 252 (1977).

[8] L. Evans and P. Bryant (editors), *LHC machine*, 2008 JINST 3 S08001.

[9] CERN Document Server, *The CERN accelerator complex - August 2018*, OPEN-PHO-ACCEL-2018-005.

[10] I. Béjar Alonso *et al.* (Eds.), *High-Luminosity Large Hadron Collider (HL-LHC): Technical design report*, CERN Yellow Reports: Monographs, CERN-2020-010 (CERN, Geneva, 2020), doi:10.23731/CYRM-2020-0010.

[11] CERN, *Ultimate HL-LHC luminosity - ions stopped after LS4*, https://lhc-commissioning.web.cern.ch/schedule/HL-LHC-plots.htm (20th Augusut 2021 accessed).

[12] P. A. Zyla *et al.* (Particle Data Group), *Prog. Theor. Exp. Phys.* 2020, 083C01 (2020) and 2021 update.

[13] G. Aad *et al.* (ATLAS Collaboration), *Combined measurements of Higgs boson production and decay using up to 80 fb^{-1} of proton-proton collision data at $\sqrt{s} = 13$ TeV collected with the ATLAS experiment*, Phys. Rev. D 101, 012002.

[14] The ATLAS Collaboration, *Combination of searches for Higgs boson pairs in pp collisions at $\sqrt{s} = 13$ TeV with the ATLAS detector*, Phys. Lett. B 800 (2020) 135103.

[15] I. Belyaev *et al.*, *The history of LHCb*, *EPJ H* 46, 3 (2021).

[16] The LHCb Collaboration, *Update of the LHCb combination of the CKM angle γ using $B \rightarrow DK$ decays*, LHCb-CONF-2018-002 (2018).

[17] The LHCb Collaboration, *Letter of Intent for the LHCb Upgrade*, CERN-LHCC-2011-001.

[18] I. Melzer-Pellmann and P. Pralavorio, *Lessons for SUSY from the LHC after the first run*, *Eur. Phys. J. C* 74, 2801 (2014).

[19] A. Bazavov *et al.*, *Equation of state and QCD transition at finite temperature*, *Phys. Rev. D* 80, 014504 (2009).

[20] T. K. NAYAK, *Heavy ions: Results from the Large Hadron Collider*, *Pramana - J Phys* 79, 719–735 (2012).

[21] David d'Enterria, *Jet quenching*, arXiv:0902.2011.

[22] The CMS Collaboration, *Study of high-p_T charged particle suppression in PbPb compared to pp collisions at $\sqrt{s_\mathrm{NN}}$ = 2.76 TeV*, *Eur. Phys. J. C* 72, 1945 (2012).

[23] JET Collaboration, *Extracting the jet transport coefficient from jet quenching in high-energy heavy-ion collisions*, *Phys. Rev. C* 90, 014909

[24] M. Asakawa and T. Hatsuda, *Jψ and η_c in the Deconfined Plasma from Lattice QCD*, *Phys. Rev. Lett.* 92, 012001.

[25] H. Satz, *Quarkonium Binding and Dissociation: The Spectral Analysis of the QGP*, *Nucl. Phys. A* (783) 249-260(2007).

[26] Ágnes Mócsy and Péter Petreczky, *Color Screening Melts Quarkonium*, *Phys. Rev. Lett.* 99 211602.

[27] The ALICE Collaboration, *Differential studies of inclusive J/ψ and ψ(2S) production at forward rapidity in Pb-Pb collisions at $\sqrt{s_\mathrm{NN}}$ = 2.76 TeV*, *J. High Energ. Phys.* 2016, 179 (2016).

[28] E. Nazarova, *Skewness of Event-by-event Elliptic Flow Fluctuations in PbPb collisions at $\sqrt{s_\mathrm{NN}}$ = 5.02 TeV with CMS*, Strangeness in Quark Matter 2017.

[29] PHENIX collaboration, *Elliptic Flow of Identified Hadrons in Au + Au Collisions at $\sqrt{s_\mathrm{NN}}$ = 200 GeV*, *Phys. Rev. Lett.* 91, 182301.

[30] ALICE collaboration, *Direct photon production in Pb–Pb collisions at $\sqrt{s_\mathrm{NN}}$ = 2.76 TeV*, *Physics Letters B* Volume 754, 10 March 2016, Pages 235-248.

[31] Stefano Trogolo for the ALICE Collaboration, *D-meson production in Pb–Pb collisions with ALICE at the LHC*, *Nucl. Phys. A* 1005 (2021) 121747.

[32] ALICE Collaboration, *The ALICE experiment at the CERN LHC*, 2008 *JINST* 3 S08002.

[33] ALICE collaboration, *ALICE trigger data-acquisition high-level trigger and control system : Technical Design Report*, CERN-LHCC-2003-062; ALICE-TDR-10.

[34] ALICE Collaboration, *Upgrade of the ALICE Experiment: Letter Of Intent*, 2014 *J. Phys. G: Nucl. Part. Phys.* 41 087001.

[35] ALICE Collaboration, *Technical Design Report for the Upgrade of the ALICE Inner Tracking System*, CERN-LHCC-2013-024; ALICE-TDR-017.

[36] W. Snoeys, *CMOS monolithic active pixel sensors for high energy physics*, *Nucl. Instrum. Methods Phys. Res. Sect. A: Accel. Spectromet. Detect. Assoc. Equip.* 765 (2014) 167–171; hSTD-9 2013—Proceedings of the 9th International Hiroshima Symposium on Development and Application of Semiconductor Tracking Detectors, International Conference Center, Hiroshima, Japan, 2–5 September 2013.

[37] M. Mager, *ALPIDE, the monolithic active pixel sensor for the ALICE ITS upgrade*, *Nucl. Instrum. Meth. A* 824 (2016) 434.

[38] ALICE collaboration, *The ALPIDE pixel sensor chip for the upgrade of the ALICE Inner Tracking System*, *Nucl. Instrum. Meth. A* 845 (2017) 583.

[39] ALICE Collaboration, *Addendum to the Technical Design Report for the Upgrade of the ALICE Time Projection Chamber*, CERN-LHCC-2015-002; ALICE-TDR-016-ADD-1.

[40] ALICE Collaboration, *Technical Design Report for the Upgrade of the Online-Offline Computing System*, CERN-LHCC-2015-006; ALICE-TDR-019.

[41] ALICE Collaboration, *Addendum of the Letter of Intent for the upgrade program of the ALICE experiment: The Muon Forward Tracker*, CERN-LHCC-2013-014; LHCC-I-022-ADD-1.

[42] ALICE Collaboration, *Technical Design Report for the Muon Forward Tracker*, CERN-LHCC-2015-001; ALICE-TDR-018.

[43] ALICE collaboration, *ALICE dimuon forward spectrometer: Technical Design Report*, CERN-LHCC-99-022; ALICE-TDR-5 (1999).

[44] ALICE collaboration, *Addendum to the Technical Design Report of the dimuon forward spectrometer*, CERN-LHCC-2000-046, ALICE-TDR-5-add-1 (2000).

[45] LHCb Collaboration, *The LHCb Detector at the LHC*, 2008 *JINST* 3 S08005.

[46] D. H. Campora Perez *et al.*, *The 40 MHz trigger-less DAQ for the LHCb Upgrade*, *Nucl. Instrum. Methods Phys. Res. A* 824 (2016) 280–283.

[47] V. V. Gligorov and E. Rodrigues, *RTA and DPA dataflow diagrams for Run 1, Run 2, and the upgraded LHCb detector*, LHCb-FIGURE-2020-016.

[48] LHCb Collaboration, *LHCb Tracker Upgrade Technical Design Report*, CERN-LHCC-2014-001; LHCB-TDR-015.

[49] LHCb Collaboration, *LHCb VELO Upgrade Technical Design Report*, CERN-LHCC-2013-021; LHCB-TDR-013.

[50] LHCb Collaboration, *LHCb PID Upgrade Technical Design Report*, CERN-LHCC-2013-022; LHCB-TDR-014.

[51] R. Aaij *et al.*, *Design and performance of the LHCb trigger and full real-time reconstruction in Run 2 of the LHC*, 2019 *JINST* 14 P04013.

[52] ATLAS Collaboration, *The ATLS Experiment at the CERN Large Hadron Collider*, 2008 *JINST* 3 S08003.

[53] J. Pequenao, *Computer generated image of the whole ATLAS detector*, CERN Document Server, CERN-GE-0803012-02.

[54] ATLAS Collaboration. *Letter of Intent for the Phase-II Upgrade of the ATLAS Experiment*, CERN-2012-022; LHCC-I-023.

[55] ATLAS Collaboration. *ATLAS Phase-II Upgrade Scoping Document*, CERN-LHCC-2015-020; LHCC-G-166.

[56] ATLAS Collaboration. *Technical Design Report for the ATLAS Inner Tracker Pixel Detector*, CERN-LHCC-2017-021; ATLAS-TDR-030.

[57] ATLAS Collaboration. *Technical Design Report for the ATLAS Inner Tracker Strip Detector*, CERN-LHCC-2017-005; ATLAS-TDR-025.

[58] ATLAS Collaboration. *ATLAS Liquid Argon Calorimeter Phase-II Upgrade : Technical Design Report*, CERN-LHCC-2017-018; ATLAS-TDR-027.

[59] ATLAS Collaboration. *Technical Design Report for the Phase-II Upgrade of the ATLAS Tile Calorimeter*, CERN-LHCC-2017-019; ATLAS-TDR-028.

[60] ATLAS Collaboration. *Technical Design Report for the Phase-II Upgrade of the ATLAS Muon Spectrometer*, CERN-LHCC-2017-017; ATLAS-TDR-026.

[61] ATLAS Collaboration. *Technical Design Report for the Phase-II Upgrade of the ATLAS Trigger and Data Acquisition System*, CERN-LHCC-2017-020; ATLAS-TDR-029.

[62] CMS Collaboration, *The CMS experiment at the CERN LHC*, 2008 *JINST* 3 S08004.

[63] CMS Collaboration, *CMS Phase II Upgrade Scope Document*, CERN-LHCC-2015-019; LHCC-G-165.

[64] CMS Collaboration, *The Phase-2 Upgrade of the CMS Tracker*, CERN-LHCC-2017-009; CMS-TDR-014.

[65] CMS Collaboration, *The Phase-2 Upgrade of the CMS Barrel Calorimeters*, CERN-LHCC-2017-011; CMS-TDR-015.

[66] CMS Collaboration, *The Phase-2 Upgrade of the CMS Endcap Calorimeter*, CERN-LHCC-2017-023; CMS-TDR-019.

[67] CMS Collaboration, *Technical proposal for a MIP timing detector in the CMS experiment Phase 2 upgrade*, CERN-LHCC-2017-027; LHCC-P-009.

[68] CMS Collaboration, *A MIP Timing Detector for the CMS Phase-2 Upgrade*, CERN-LHCC-2019-003; CMS-TDR-020.

[69] CMS Collaboration, *The Phase-2 Upgrade of the CMS Muon Detectors*, CERN-LHCC-2017-012; CMS-TDR-016.

[70] CMS Collaboration, *Technical Proposal for the Phase-II Upgrade of the CMS Detector*, CERN-LHCC-2015-010; LHCC-P-008; CMS-TDR-15-02.

[71] CMS Collaboration, *The Phase-2 Upgrade of the CMS L1 Trigger Interim Technical Design Report*, CERN-LHCC-2017-013; CMS-TDR-017.

[72] CMS Collaboration, *The Phase-2 Upgrade of the CMS Level-1 Technical Design Report*, CERN-LHCC-2020-004: CMS-TDR-021.

[73] CMS Collaboration, *The Phase-2 Upgrade of the CMS DAQ Interim Technical Design*, CERN-LHCC-2017-014; CMS-TDR-018.

[74] CMS Collaboration, *The Phase-2 Upgrade of the CMS Data Acquisition and High Level Trigger Technical Design Report*, CERN-LHCC-2021-007; CMS-TDR-022.

[75] D. Bertolini *et al.*, *Pileup per particle identification*, J. High Energ. Phys. 2014, 59 (2014). (https://doi.org/10.1007/JHEP10(2014)059)

[76] C. Fitzpatrick, *Too much of a good thing: How to trigger in a signal-rich environment*, EP-IT Data science seminars, CERN, 13th December 2017.

[77] Siemens SIMATIC WinCC OA, https://www.winccoa.com.

[78] P. Chochula *et al.*, *Challenges of the ALICE Detector Control System for the LHC RUN3*, ICALEPCS 2017, Barcelona, Spain, pp. 323-327.

[79] J. Lång *et al.*, *ADAPOS: An Architecture for Publishing ALICE DCS Conditions Data*, ICALEPCS 2017, Barcelona, Spain, pp. 482-485.

[80] O. Holme, M. González-Berges, P. Golonka, and S. Schmeling, *The JCOP Framework*, Tech. Rep. CERN-OPEN-2005-027, CERN, Geneva (2005).

[81] CAEN, https://www.caen.it.

[82] K. Yamakawa *et al.*, *Design and implementation of detector control system for muon forward tracker at ALICE*, 2020 *JINST* 15 T10002.

Acronyms

ADAPOS ALICE datapoint service
AGS alternating gradient synchrotron
ALF ALICE low-level front-end
ALICE a large ion collider experiment
ALPIDE ALICE pixel detector
ATLAS a toroidal LHC apparatus

BC barrel calorimeter
BCT barrel calorimeter trigger
BMTF barrel muon track finder
BNL Brookhaven national laboratory

CMS compact muon solenoid
CRU common readout unit
CSC cathode strip chamber
CT correlator trigger
CTP central trigger processor

DAQ data acquisition system
DCS detector control system
DT drift tube

EASY embedded assembly system
EB endcap barrel
ECAL electromagnetic calorimeter
ECal electromagnetic calorimeter
EMTF endcap muon track finder
EPN event processor node

FEE frontend electronics
FLP first level processor
FPGA field programmable gate array
FRED front-end device
FSM finite state machine

GBT giga-bit transceiver
GBT-SCA GBT slow control adaptor
GCT global calorimeter trigger
GEM gas electron multiplier

GUI	graphical user interface
HCAL	hadron calorimeter
HCal	hadron calorimeter
HF	hadron forward calorimeter
HGCAL	high-granularity calorimeter
HL-LHC	high-luminosity LHC
HLT	high-level trigger
HTT	hardware-based tracking for the trigger
iRPC	improved resistive plate chamber
IT	inner tracker
ITS	inner tracking system
JCOP	joint control project
L0	Level-0 trigger
L1	Level-1 trigger
LAr	liquid-argon calorimeter
LB	long barrel
LBNL	Lawrence Berkeley National Laboratory
LHC	large hadron collider
LHCb	large hadron collider beauty
LINAC	linear accelerator
MAPS	CMOS monolithic active pixel sensor
MDT	monitor drift tube
MFT	muon forward tracker
MIP	minimum ionizing particle
NSW	new small wheel
O^2	online-offline computing system
OMTF	overlap muon track finder
OT	outer tracker
PHENIX	pioneering high-energy nuclear interaction experiment
PID	particle identification
PLC	programmable logic controller
PSU	power supply unit
QCD	quantum chromodynamics
QGP	quark-gluon plasma
RHIC	relativistic heavy ion collider

RICH	ring-imaging Cherenkov detector
RPC	resistive plate chamber
RU	readout unit
SCADA	supervisory control and data acquisition
SPS	super proton synchrotron
STAR	solenoid tracker at RHIC
SUSY	supersymmetry
TGC	thin gap chambers
TPC	time projection chamber
TT	trigger tracker
VELO	vertex locator
WinCC OA	WinCC open architecture